

A 3-D Geometry-Based Stochastic Model for Unmanned Aerial Vehicle MIMO Ricean Fading Channels

Xiang Cheng¹, Senior Member, IEEE, Yiran Li², Cheng-Xiang Wang³, Fellow, IEEE,
Xuefeng Yin⁴, Member, IEEE, and David W. Matolak⁵, Senior Member, IEEE

Abstract—In this article, we propose a novel 3-D geometry-based stochastic model (GBSM), i.e., a two-cylinder model, for unmanned aerial vehicle (UAV) multiple-input–multiple-output (MIMO) Ricean fading channels. The received signal is a sum of the Line-of-Sight (LoS) component, single-bounced (SB) rays at the UAV side, SB rays at the ground station side, SB rays on the ground, and double-bounced rays. This makes our model adaptable to a wide variety of UAV communication scenarios. More importantly, the proposed UAV model is the first two-cylinder model that considers ground reflections. Moreover, our model has the ability to investigate the impact of some unique UAV-related parameters (e.g., the UAV’s moving direction, UAV’s altitude, and antenna orientation) on channel characteristics in a 3-D nonisotropic propagation environment. From the proposed model, we derive and study some significant statistical properties, including the space-time correlation function (CF), Doppler power spectral density (PSD), envelope level crossing rate (LCR), and average fade duration (AFD). Some numerical results and interesting observations are provided, which can be considered useful guidance for the design of UAV-MIMO communication

systems. Finally, the utility of our model is verified by the close agreement between the theoretical results and some example measurement data.

Index Terms—3-D geometry-based stochastic model (GBSM), multiple-input–multiple-output (MIMO), Ricean fading, statistical properties, unmanned aerial vehicle (UAV) channel modeling.

I. INTRODUCTION

UNMANNED aerial vehicle (UAV) communication has been applied in a variety of fields due to its low cost and high flexibility. The use of UAVs has attracted widespread attention, and interest and applications are expected to grow in the near future [1]–[5]. Compared with conventional cellular and vehicular communications, UAV communications exhibit some unique propagation features. For example, UAVs are able to move in a 3-D space with relatively high velocities and this high mobility in a 3-D space is a significant new factor in channel characterization when the UAV itself is near obstacles since traditional air–ground communications typically have the aircraft well clear of any terrestrial obstacles. Therefore, the impact of channel characteristics on the small UAV communication system design is important. As is known, multiple-input–multiple-output (MIMO) antenna systems have been identified as a technology that can effectively improve communication performance. Such systems have been widely accepted and are used in many standards, e.g., the long-term evolution (LTE) 4G standard. More recently, the so-called “massive” MIMO, which is considered to be an important technical feature for 5G communication [6], [7], has been extensively studied. Therefore, recent research on the investigation of MIMO in UAV communication systems has grown. Yet due to the unique propagation features of UAV communications, whether MIMO is suitable for real UAV communications and how MIMO works for a range of UAV scenarios are still open and interesting problems.

Measuring the communication environment and constructing an easy-to-use channel model is an important early step in designing a wireless communication system effectively. Presently, many research groups have studied UAV measurement [8]–[20] and UAV channel modeling [17]–[26] for UAV channel characterization. These UAV channel models can be divided into deterministic models and stochastic models, and

Manuscript received December 12, 2019; revised March 4, 2020 and April 17, 2020; accepted May 10, 2020. Date of publication May 19, 2020; date of current version September 15, 2020. This work was supported in part by the National Key Research and Development Program of China under Grant 2018YFB1801101; in part by the National Natural Science Foundation of China under Grant 6196206006 and Grant 61971313; in part by the High-Level Innovation and Entrepreneurial Research Team Program in Jiangsu; in part by the High-Level Innovation and Entrepreneurial Talent Introduction Program in Jiangsu; in part by the Research Fund of National Mobile Communications Research Laboratory, Southeast University, under Grant 2020B01; in part by the Huawei Cooperation Project; in part by the EU H2020 RISE TESTBED2 Project under Grant 872172; and in part by the Open Research Fund of Key Laboratory of Wireless Sensor Network and Communication under Grant 2017003, through the Shanghai Institute of Microsystem and Information Technology, Chinese Academy of Sciences. (Corresponding author: Xiang Cheng.)

Xiang Cheng and Yiran Li are with the State Key Laboratory of Advanced Optical Communication Systems and Networks, Department of Electronics, School of Electronics Engineering and Computer Science, Peking University, Beijing 100871, China, and also with the Key Laboratory of Wireless Sensor Network and Communication, Shanghai Institute of Microsystem and Information Technology, Chinese Academy of Sciences, Shanghai 200050, China (e-mail: xiangcheng@pku.edu.cn; yiran.li@pku.edu.cn).

Cheng-Xiang Wang is with the National Mobile Communications Research Laboratory, School of Information Science and Engineering, Southeast University, Nanjing 210096, China, and also with the Pervasive Communication Research Center, Purple Mountain Laboratories, Nanjing 211111, China (e-mail: chxwang@seu.edu.cn).

Xuefeng Yin is with the College of Electronics and Information Engineering, Tongji University, Shanghai 201804, China (e-mail: yinxuefeng@tongji.edu.cn).

David W. Matolak is with the Department of Electrical Engineering, University of South Carolina, Columbia, SC 29208 USA (e-mail: matolak@cec.sc.edu).

Digital Object Identifier 10.1109/IIOT.2020.2995707

the latter can be further classified as nongeometrical stochastic models (NGSMs) and geometry-based stochastic models (GBSMs).

Daniel *et al.* [21], Wu *et al.* [22], and Shi *et al.* [23] developed deterministic UAV models using the ray-tracing or the finite-difference time-domain (FDTD) method. The ray-tracing method is a radio propagation simulation of the actual environment, based on some basic rules of wave propagations. In contrast, the FDTD method was invented for obtaining discrete solutions to Maxwell's equations, providing information about the propagation of electromagnetic waves. These deterministic modeling approaches usually have high accuracy but require numerous physical data and time-consuming calculations to characterize a particular propagation environment. Therefore, the generality of these approaches is limited.

Compared with deterministic models, stochastic models' generality is higher and the corresponding complexity is lower, along with acceptable accuracy. As mentioned, they can be classified as NGSMs or GBSMs, depending on whether or not a geometrical shape with effective scatterers is used. One widely used NGSM for UAV channels is a purely statistical model [24], [25], in which the channel amplitude is a stochastic process. This kind of model can be useful for the UAV system design but may not be sufficiently accurate [27].

Recently, a new set of UAV channel models, based upon a large set of measurement data, has been proposed in [17]–[20]. These models always include intermittent multipath components (MPCs), an Earth surface reflection, and a Line-of-Sight (LoS) component. The first two components are derived from geometry and are hence largely deterministic, whereas the intermittent MPCs are described statistically. These models can be considered hybrid deterministic stochastic or partially geometry based; the deterministic portion is a two-ray (2R) model. Considering that Earth curvature cannot be neglected in the case of long-range UAV communication, the authors provide a curved-Earth 2R (CE2R) model version. This model, along with its flat-Earth (FE2R) counterpart, can be useful under scenarios where an Earth surface reflection is present and can be received.

Unlike NGSMs, the method adopted by GBSMs is to model the channel by assuming the distribution of scatterers directly, which can effectively reduce the complexity of the channel modeling process. For terrestrial vehicle-to-vehicle (V2V) communication, GBSM methods have been widely used for channel modeling [28]–[34]. Based on GBSMs, these papers have drawn some useful conclusions regarding the impact of vehicular traffic density and some other parameters. Similar to vehicular communications, UAV communications exhibit rapidly varying and complicated time-variant propagation characteristics. Hence, research on UAV channel modeling using GBSMs has gradually increased in recent years. A 3-D narrowband one-cylinder UAV GBSM was developed in [35] and [36], which has been extended to a wideband one-concentric-cylinder UAV model in [37] recently. Jin *et al.* [38] proposed a 3-D one-sphere UAV model for narrowband communication channels. However, these GBSMs assumed there are no scatterers around the UAV, i.e., a high-altitude UAV

communication scenario. Moreover, only a few channel properties were investigated for single-bounced (SB) rays.

This article develops a generic narrowband UAV model, i.e., a two-cylinder reference model, where the received signal is a superposition of the LoS component, SB rays from scatterers around the UAV (SB-U), SB rays from scatterers around the ground station (SB-G), SB rays from the ground reflection (SB-GR), and double-bounced (DB) rays. For simplicity here, this model does not account for aircraft pitch and roll maneuvers, which will be a subject for future investigation. Note that compared with existing two-cylinder models [28]–[30], the proposed two-cylinder model for the first time considers the ground reflection, which has a significant impact on UAV channels as shown in many UAV channel measurements [8]–[20]. Overall, the contributions and novelties of this article are summarized as follows.

- 1) We propose a generic GBSM, consisting of the sum of the LoS component, SB, and DB rays, for narrowband nonisotropic UAV-MIMO Ricean fading channels. The proposed model is adaptive to a wide variety of scenarios by adjusting model parameters, e.g., UAV's moving direction and UAV's elevation angle and antenna orientation.
- 2) Unlike other GBSMs for conventional cellular and vehicular communications, the proposed UAV-MIMO GBSM considers unique properties of UAV propagations, e.g., significant ground reflection, large altitude difference between UAV and ground station (GS), and the UAV movement in a 3-D space. Therefore, the proposed UAV model is the first two-cylinder model that considers ground reflections. Moreover, by considering unique geometry properties of our model, a new generic relationship between the Angle of Arrival (AoA) and Angle of Departure (AoD) is derived.
- 3) From the proposed model, we derive the expressions of the space-time correlation function (CF), Doppler power spectrum density (PSD), envelope level crossing rate (LCR), and average fade duration (AFD).
- 4) We present some interesting and useful observations based on the proposed model's channel statistic. Finally, a good match between the theoretical results of the statistical properties of the model and the measurement data in [24] and [39] demonstrates the utility of the proposed model.

The remainder of this article is outlined as follows. Section II describes the novel GBSM for UAV-MIMO Ricean fading channels. In Section III, from the proposed model, the space-time CF, Doppler PSD, envelope LCR, and AFD are derived. Section IV presents some numerical results and interesting observations. Finally, conclusions are drawn in Section V.

II. NOVEL GBSM FOR UAV-MIMO RICEAN FADING CHANNELS

In this article, we consider a narrowband single-user UAV-MIMO communication system with M_T UAV and M_R GS antenna elements. Both the UAV and the GS are in motion.

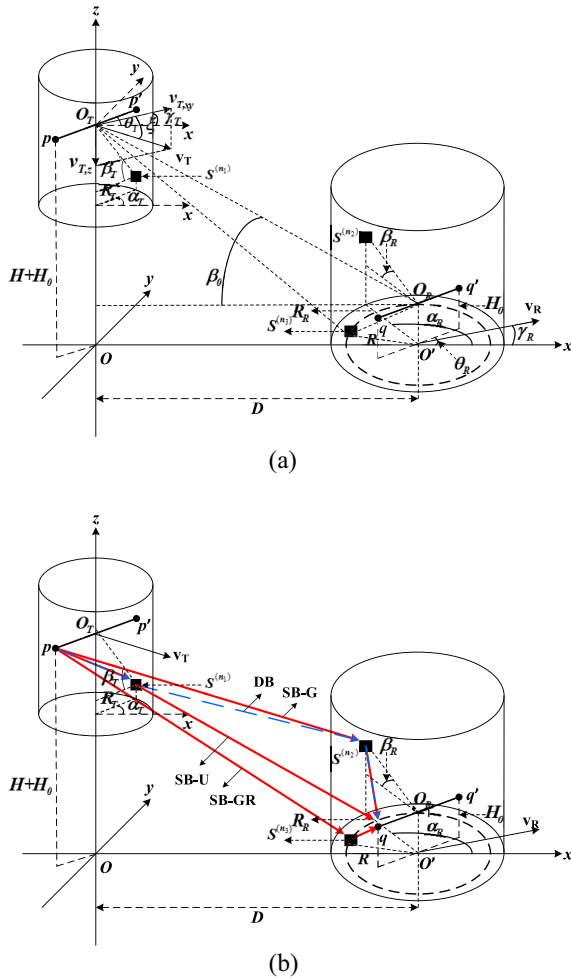


Fig. 1. (a) Generic channel model with UAV-MIMO channels ($M_T = M_R = 2$). (b) Specific path information of SB and DB rays in the proposed model (red solid line: SB rays and blue dotted line: DB rays).

The geometry of the proposed narrowband two-cylinder UAV-GBSM is shown in Fig. 1, where $M_T = M_R = 2$. We assume that the two cylinders are located around the UAV and the GS and that the effective scatterers are distributed on them. Note that here these scatterers located on the two cylinders are the so-called effective scatterers, which could include the impact of the UAV and GS themselves. We suppose there are N_1 effective scatterers around the UAV lying on the surface of a cylinder of radius R_T , and the n_1 th ($n_1 = 1, 2, \dots, N_1$) effective scatterer is denoted by $s^{(n_1)}$. Similarly, suppose there are N_2 effective scatterers around the GS lying on the surface of a cylinder of radius R_R , and the n_2 th ($n_2 = 1, 2, \dots, N_2$) effective scatterer is denoted by $s^{(n_2)}$. We assume that the ground reflection occurs on the bottom surface of the cylinder at the GS. We suppose there are N_3 effective scatterers lying on the underside of the cylinder of radius $0 \leq R \leq R_R$ around the GS, and the n_3 th ($n_3 = 1, 2, \dots, N_3$) effective scatterer is denoted by $s^{(n_3)}$. The height of the GS is denoted H_0 . The vertical and horizontal distance between the UAV and GS are H and D , respectively, and satisfy $D \gg R_T/R_R$. Parameters δ_T and δ_R are used to present antenna spacings at the UAV and GS. In addition, the direction of two antenna arrays is denoted

by θ_T and θ_R , relative to the x -axis. For simplicity here, we keep the arrays parallel to the x - y plane, hence we do not account for aircraft pitch and roll maneuvers, and this is a subject for future investigation. We assume the UAV and GS move with speeds of v_T and v_R , respectively. As shown in Fig. 1, we decompose the vector v_T into a horizontal component $v_{T,xy}$ and a perpendicular component $v_{T,z}$, and then define $[v_{T,xy}, v_T] = \xi$, and $[v_{T,xy}, +x] = \gamma_T$, where $[\cdot, \cdot]$ denotes the included angle. This angle pair ξ and γ_T is used to characterize the UAV movement in a 3-D space. For the GS, it moves in the direction of γ_R in the xy plane. The AoA of the wave traveling from an effective scatterer $s^{(n_i)}$ ($i = 1, 2, 3$) toward the GS is denoted by $\alpha_R^{(n_i)}$ and $\beta_R^{(n_i)}$, and the AoD of the wave that impinges on the effective scatterer $s^{(n_i)}$ is designated by $\alpha_T^{(n_i)}$ and $\beta_T^{(n_i)}$. Parameters α_T^{LoS} , β_T^{LoS} , α_R^{LoS} , and β_R^{LoS} denote AoAs and AoDs of the LoS path, which are omitted in Fig. 1 to avoid the figure being overcrowded.

From Fig. 1, we can see that at the carrier frequency f_c , the received complex fading envelope between the p th ($p = 1, \dots, M_T$) UAV antenna and the q th ($q = 1, \dots, M_R$) GS antenna is a superposition of the LoS [i.e., $T_p - R_q$], SB-U [i.e., $T_p - s^{(n_1)} - R_q$], SB-G [i.e., $T_p - s^{(n_2)} - R_q$], SB-GR [i.e., $T_p - s^{(n_3)} - R_q$], and DB [i.e., $T_p - s^{(n_1)} - s^{(n_2)} - R_q$] rays, which can be expressed as

$$h_{pq}(t) = h_{pq}^{\text{LoS}}(t) + h_{pq}^{\text{SB-U}}(t) + h_{pq}^{\text{SB-G}}(t) + h_{pq}^{\text{SB-GR}}(t) + h_{pq}^{\text{DB}}(t) \quad (1)$$

where

$$h_{pq}^{\text{LoS}}(t) = \sqrt{\frac{K\Omega_{pq}}{K+1}} e^{-j2\pi f_c \tau_{pq}} e^{j2\pi f_T m t [\cos(\alpha_T^{\text{LoS}} - \gamma_T) \cos \beta_T^{\text{LoS}} \cos \xi + \sin \beta_T^{\text{LoS}} \sin \xi]} e^{j2\pi f_R m t [\cos(\alpha_R^{\text{LoS}} - \gamma_R) \cos \beta_R^{\text{LoS}}]} \quad (2)$$

$$h_{pq}^{\text{SB-U}}(t) = \sqrt{\frac{\eta_{\text{SB-U}} \Omega_{pq}}{K+1}} \lim_{N_1 \rightarrow \infty} \frac{1}{\sqrt{N_1}} \sum_{n_1=1}^{N_1} e^{j\phi^{(n_1)}} e^{-2\pi f_c \tau_{pq, n_1}} e^{j2\pi f_T m t [\cos(\alpha_T^{(n_1)} - \gamma_T) \cos \beta_T^{(n_1)} \cos \xi + \sin \beta_T^{(n_1)} \sin \xi]} e^{j2\pi f_R m t [\cos(\alpha_R^{(n_1)} - \gamma_R) \cos \beta_R^{(n_1)}]} \quad (3)$$

$$h_{pq}^{\text{SB-G}}(t) = \sqrt{\frac{\eta_{\text{SB-G}} \Omega_{pq}}{K+1}} \lim_{N_2 \rightarrow \infty} \frac{1}{\sqrt{N_2}} \sum_{n_2=1}^{N_2} e^{j\phi^{(n_2)}} e^{-2\pi f_c \tau_{pq, n_2}} e^{j2\pi f_T m t [\cos(\alpha_T^{(n_2)} - \gamma_T) \cos \beta_T^{(n_2)} \cos \xi + \sin \beta_T^{(n_2)} \sin \xi]} e^{j2\pi f_R m t [\cos(\alpha_R^{(n_2)} - \gamma_R) \cos \beta_R^{(n_2)}]} \quad (4)$$

$$h_{pq}^{\text{SB-GR}}(t) = \sqrt{\frac{\eta_{\text{SB-GR}} \Omega_{pq}}{K+1}} \lim_{N_3 \rightarrow \infty} \frac{1}{\sqrt{N_3}} \sum_{n_3=1}^{N_3} e^{j\phi^{(n_3)}} e^{-2\pi f_c \tau_{pq, n_3}} e^{j2\pi f_T m t [\cos(\alpha_T^{(n_3)} - \gamma_T) \cos \beta_T^{(n_3)} \cos \xi + \sin \beta_T^{(n_3)} \sin \xi]} e^{j2\pi f_R m t [\cos(\alpha_R^{(n_3)} - \gamma_R) \cos \beta_R^{(n_3)}]} \quad (5)$$

$$h_{pq}^{\text{DB}}(t) = \sqrt{\frac{\eta_{\text{DB}} \Omega_{pq}}{K+1}} \lim_{N_1, N_2 \rightarrow \infty} \frac{1}{\sqrt{N_1 N_2}} \sum_{n_1, n_2=1}^{N_1, N_2} e^{j\phi^{(n_1, n_2)}} e^{-2\pi f_c \tau_{pq, n_1, n_2}}$$

$$\begin{aligned} & e^{j2\pi f_{Tm}t} \left[\cos(\alpha_T^{(n1)} - \gamma_T) \cos \beta_T^{(n1)} \cos \xi + \sin \beta_T^{(n1)} \sin \xi \right] \\ & e^{j2\pi f_{Rm}t} \left[\cos(\alpha_R^{(n2)} - \gamma_R) \cos \beta_R^{(n2)} \right]. \end{aligned} \quad (6)$$

In (2)–(6), $\tau_{pq} = \varepsilon_{pq}/c$, $\tau_{pq,n1} = (\varepsilon_{pn1} + \varepsilon_{n1q})/c$, $\tau_{pq,n2} = (\varepsilon_{pn2} + \varepsilon_{n2q})/c$, $\tau_{pq,n3} = (\varepsilon_{pn3} + \varepsilon_{n3q})/c$, and $\tau_{pq,n1,n2} = (\varepsilon_{pn1} + \varepsilon_{n1n2} + \varepsilon_{n2q})/c$ are propagation times of waves through the link $T_p - R_q$, $T_p - s^{(n1)} - R_q$, $T_p - s^{(n2)} - R_q$, $T_p - s^{(n3)} - R_q$, and $T_p - s^{(n1)} - s^{(n2)} - R_q$, respectively, where symbols ε_{pq} , ε_{pn1} , ε_{n1q} , ε_{pn2} , ε_{n2q} , ε_{pn3} , ε_{n3q} , and ε_{n1n2} denote distances $T_p - R_q$, $T_p - s^{(n1)}$, $s^{(n1)} - R_q$, $T_p - s^{(n2)}$, $s^{(n2)} - R_q$, $T_p - s^{(n3)}$, $s^{(n3)} - R_q$, and $T_p - s^{(n1)} - s^{(n2)} - R_q$, respectively. c is the speed of the light. The received total power and the Ricean factor are expressed by Ω_{pq} and K_{pq} , respectively. In addition, η_{SB-U} , η_{SB-G} , η_{SB-GR} , and η_{DB} are energy-related parameters, which represent the ratio of SB and DB components to the total scattered power $\Omega_{pq}/(K+1)$, and satisfy $\eta_{SB-U} + \eta_{SB-G} + \eta_{SB-GR} + \eta_{DB} = 1$. The scattering caused phases $\phi^{(n1)}$, $\phi^{(n2)}$, $\phi^{(n3)}$, and $\phi^{(n1,n2)}$ are independent random variables, and all are uniformly distributed over $[-\pi, \pi)$. f_{Tm} and f_{Rm} donate maximum Doppler frequencies of the UAV and the GS, respectively. It is worth noting that although the limiting case (N_1 , N_2 , and N_3 going to infinity) we model here is artificial, some researchers find this of utility. It also simplifies the mathematics via the central limit theorem and enables some closed-form results that can provide insight when components' number is indeed large.

Based on the spatial distance formula, distances between the scatterer and antenna ε_{pq} , ε_{pn1} , ε_{n1q} , ε_{pn2} , ε_{n2q} , ε_{pn3} , and ε_{n3q} can be expressed as

$$\varepsilon_{pq} = \sqrt{(D_x^T - D_x^R)^2 + (D_y^T - D_y^R)^2 + (D_z^T - D_z^R)^2} \quad (7)$$

$$\varepsilon_{pn1} = \sqrt{(D_x^T - D_x^{n1})^2 + (D_y^T - D_y^{n1})^2 + (D_z^T - D_z^{n1})^2} \quad (8)$$

$$\varepsilon_{n1q} = \sqrt{(D_x^{n1} - D_x^R)^2 + (D_y^{n1} - D_y^R)^2 + (D_z^{n1} - D_z^R)^2} \quad (9)$$

$$\varepsilon_{pn2} = \sqrt{(D_x^T - D_x^{n2})^2 + (D_y^T - D_y^{n2})^2 + (D_z^T - D_z^{n2})^2} \quad (10)$$

$$\varepsilon_{n2q} = \sqrt{(D_x^{n2} - D_x^R)^2 + (D_y^{n2} - D_y^R)^2 + (D_z^{n2} - D_z^R)^2} \quad (11)$$

$$\varepsilon_{pn3} = \sqrt{(D_x^T - D_x^{n3})^2 + (D_y^T - D_y^{n3})^2 + (D_z^T - D_z^{n3})^2} \quad (12)$$

$$\varepsilon_{n3q} = \sqrt{(D_x^{n3} - D_x^R)^2 + (D_y^{n3} - D_y^R)^2 + (D_z^{n3} - D_z^R)^2} \quad (13)$$

where the parameters $D_{x/y/z}^{n_i}$ denote the position coordinates of scatterers $s^{(n_i)}$ in the 3-D coordinate axis along the $x/y/z$ -axis, respectively. Parameters $D_{x/y/z}^T$ and $D_{x/y/z}^R$ denote the position coordinates of Tx and Rx in the 3-D coordinate axis along the $x/y/z$ -axis, respectively. They can be specifically expressed as $D_x^{n1} = R_T \cos \alpha_T^{(n1)}$, $D_y^{n1} = R_T \sin \alpha_T^{(n1)}$, $D_z^{n1} = R_T \tan \beta_T^{(n1)}$, $D_x^{n2} = D + R_R \cos \alpha_R^{(n2)}$, $D_y^{n2} = R_R \sin \alpha_R^{(n2)}$, $D_z^{n2} = R_R \tan \beta_R^{(n2)}$, $D_x^{n3} = D + R \cos \alpha_R^{(n3)}$, $D_y^{n3} = R \sin \alpha_R^{(n3)}$, $D_z^{n3} = 0$, $D_x^T = \Delta_T \cos \theta_T$, $D_y^T = \Delta_T \sin \theta_T$, $D_z^T = D \tan \beta_0 + H_0$, $D_x^R = D + \Delta_R \cos \theta_R$, $D_y^R = \Delta_R \sin \theta_R$, and $D_z^R = H_0$. The parameter Δ_T is the distance between the

p th UAV antenna element and the center of the UAV antenna array, whereas the parameter Δ_R is the distance between the q th GS antenna element and the center of the GS antenna array. For the uniform linear antenna arrays (ULAs), they are defined as

$$\Delta_T = \frac{1}{2}(M_T + 1 - 2p)\delta_T \quad (14)$$

$$\Delta_R = \frac{1}{2}(M_R + 1 - 2q)\delta_R. \quad (15)$$

For SB rays, AoD and AoA have a certain geometric relationship and can be converted to each other, which can be expressed as follows. The detailed derivation is in Appendix A.

A. For SB-U Rays

$$\cos \alpha_R^{(n1)} \approx -1 \quad (16)$$

$$\sin \alpha_R^{(n1)} \approx \frac{\frac{R_T}{D} \sin \alpha_T^{(n1)}}{1 - \frac{R_T}{D} \cos \alpha_T^{(n1)}} \quad (17)$$

$$\cos \beta_R^{(n1)} \approx \cos \beta_0 + \frac{R_T}{D} \sin \beta_0 \cos \beta_0 A_T^{(n1)} \quad (18)$$

$$\sin \beta_R^{(n1)} \approx \sin \beta_0 - \frac{R_T}{D} \cos^2 \beta_0 A_T^{(n1)} \quad (19)$$

where $A_T^{(n1)} = \tan \beta_T^{(n1)} \cos \beta_0 - \cos \alpha_T^{(n1)} \sin \beta_0$.

B. For SB-G Rays

$$\cos \alpha_T^{(n2)} \approx 1 \quad (20)$$

$$\sin \alpha_T^{(n2)} \approx \frac{\frac{R_R}{D} \sin \alpha_R^{(n2)}}{1 + \frac{R_R}{D} \cos \alpha_R^{(n2)}} \quad (21)$$

$$\cos \beta_T^{(n2)} \approx \cos \beta_0 + \frac{R_R}{D} \sin \beta_0 \cos \beta_0 A_R^{(n2)} \quad (22)$$

$$\sin \beta_T^{(n2)} \approx \sin \beta_0 - \frac{R_R}{D} \cos^2 \beta_0 A_R^{(n2)} \quad (23)$$

where $A_R^{(n2)} = \tan \beta_R^{(n2)} \cos \beta_0 + \cos \alpha_R^{(n2)} \sin \beta_0$.

C. For SB-GR Rays

$$\cos \alpha_T^{(n3)} \approx 1 \quad (24)$$

$$\sin \alpha_T^{(n3)} \approx \frac{\frac{R}{D} \sin \alpha_R^{(n3)}}{1 + \frac{R}{D} \cos \alpha_R^{(n3)}} \quad (25)$$

$$\cos \beta_T^{(n3)} \approx \cos \beta_0 - \frac{R}{D} \sin \beta_0 \cos \beta_0 A_R^{(n3)} \quad (26)$$

$$\sin \beta_T^{(n3)} \approx \sin \beta_0 + \frac{R}{D} \cos^2 \beta_0 A_R^{(n3)} \quad (27)$$

where $A_R^{(n3)} = \tan \beta_R^{(n3)} \cos \beta_0 - \cos \alpha_R^{(n3)} \sin \beta_0$.

In fact, our proposed model is a *reference* model that can be used for theoretical channel analysis. It assumes that the number of effective scatterers is infinite, i.e., $N_1, N_2, N_3 \rightarrow \infty$. In this case, we can use continuous expressions α_R , β_R and

α_T , β_T to replace discrete expressions $\alpha_R^{(n_i)}$, $\beta_R^{(n_i)}$ and $\alpha_T^{(n_i)}$, $\beta_T^{(n_i)}$, and assume azimuth angles and elevation angles are independent. Therefore, the joint PDF $f(\alpha, \beta)$ can be approximated as the product of the marginal PDFs of the azimuth angle $f(\alpha)$ and the elevation angle $f(\beta)$. Here, we use the von Mises PDF to characterize azimuth angles α_T and α_R , which is defined as

$$f(\alpha) = \frac{e^{k \cos(\alpha - \alpha_\mu)}}{2\pi I_0(k)}, \quad -\pi \leq \alpha \leq \pi \quad (28)$$

where $I_0(\cdot)$ is the zeroth-order modified Bessel function of the first kind and $\alpha_\mu \in [-\pi, \pi]$ is the mean angle at which the scatterers are distributed in the xy plane. The parameter k controls the spread around the mean angle and increasing k incurs more nonisotropic scattering. The elevation angles β_T and β_R are described by the cosine PDF [28], which is defined as

$$f(\beta) = \frac{\pi}{4\beta_m} \cos\left(\frac{\pi}{2} \frac{\beta - \beta_\mu}{\beta_m}\right), \quad |\beta - \beta_\mu| \leq \beta_m \leq \frac{\pi}{2}. \quad (29)$$

Note that $\beta \in [\beta_\mu - \beta_m, \beta_\mu + \beta_m]$. Two parameters β_m and β_μ are the maximum elevation angle and the mean angle, respectively. Here, we let $\beta_\mu - \beta_m = \beta_1$ and $\beta_\mu + \beta_m = \beta_2$, i.e., $\beta \in [\beta_1, \beta_2]$. Applying these PDFs to the AoA and AoD, we have

$$f(\alpha_T) = \frac{e^{k_T \cos(\alpha_T - \alpha_{T\mu})}}{2\pi I_0(k_T)}, \quad -\pi \leq \alpha_T \leq \pi \quad (30)$$

$$f(\alpha_R) = \frac{e^{k_R \cos(\alpha_R - \alpha_{R\mu})}}{2\pi I_0(k_R)}, \quad -\pi \leq \alpha_R \leq \pi \quad (31)$$

$$f(\beta_T) = \frac{\pi}{4\beta_{Tm}} \cos\left(\frac{\pi}{2} \frac{\beta_T - \beta_{T\mu}}{\beta_{Tm}}\right), \quad \beta_{T1} \leq \beta_T \leq \beta_{T2} \quad (32)$$

$$f(\beta_R) = \frac{\pi}{4\beta_{Rm}} \cos\left(\frac{\pi}{2} \frac{\beta_R - \beta_{R\mu}}{\beta_{Rm}}\right), \quad \beta_{R1} \leq \beta_R \leq \beta_{R2}. \quad (33)$$

Finally, we use the PDF $f(R) = 2R/R_R^2$ to characterize the distribution of radius R , which means scatterers $s^{(n_i)}$ have a uniform density between O' and R_R on the ground. Some important parameters are listed in Table I for ease of reference.

III. EXPRESSIONS OF CHANNEL CHARACTERISTICS

We derive some important statistical properties for the UAV-MIMO channel in this section, including the space-time CF, Doppler PSD, envelope LCR, and AFD.

A. Space-Time CF

For two arbitrary complex fading envelopes $h_{pq}(t)$ and $h_{p'q'}(t)$, the normalized space-time CF is defined as

$$R_{pq,p'q'}(\delta_T, \delta_R, \tau) = \frac{E[h_{pq}^*(t)h_{p'q'}(t + \tau)]}{\sqrt{\Omega_{pq}\Omega_{p'q'}}} \quad (34)$$

where $(\cdot)^*$ and $E[\cdot]$ denote the complex conjugate operation and the statistical expectation operator, respectively. It can be observed that (34) is a function of time separation τ , UAV side space separation δ_T , and GS side

TABLE I
DEFINITION OF SIGNIFICANT MODEL PARAMETERS

Symbol	Definition
D	The horizontal distance between the UAV and GS
H	The vertical distance between the UAV and GS
H_0	The altitude of the GS
R_T R_R	The radius of the cylinder at the UAV and GS
β_0	The elevation angle of the UAV's position
δ_T δ_R	The spacing between antenna elements at the UAV and GS
θ_T θ_R	The orientation of antenna arrays at the UAV and GS
v_T v_R	The velocity of the UAV and GS, respectively
$v_{T,xy}$ $v_{T,z}$	The horizontal and the perpendicular component of v_T
f_{Tm} f_{Rm}	The maximum Doppler shift caused by the UAV and GS
ξ	The angle between $v_{T,xy}$ and v_T
γ_T	The angle between $v_{T,xy}$ and the positive x axis
γ_R	The angle between v_R and the positive x axis
$\alpha_T^{(n_i)}$ $\beta_T^{(n_i)}$	The azimuth and elevation AoD at $s^{(n_i)}$
$\alpha_R^{(n_i)}$ $\beta_R^{(n_i)}$	The azimuth and elevation AoA from $s^{(n_i)}$
α_T^{LoS} β_T^{LoS}	The azimuth and elevation AoD of the LoS path
α_R^{LoS} β_R^{LoS}	The azimuth and elevation AoA of the LoS path
$\phi^{(n)}$	The random phase caused by scattering at $s^{(n_i)}$
$\alpha_{R\mu}$ k_R	The parameters in the PDF of the azimuth AoA
$\beta_{R\mu}$ β_{Rm}	The parameters in the PDF of the elevation AoA
$\alpha_{T\mu}$ k_T	The parameters in the PDF of the azimuth AoD
$\beta_{T\mu}$ β_{Tm}	The parameters in the PDF of the elevation AoD

space separation δ_R . Note that (34) can be divided into five components

$$R_{pq,p'q'}(\delta_T, \delta_R, \tau) = R_{pq,p'q'}^{LoS}(\delta_T, \delta_R, \tau) + R_{pq,p'q'}^{SB-U}(\delta_T, \delta_R, \tau) + R_{pq,p'q'}^{SB-G}(\delta_T, \delta_R, \tau) + R_{pq,p'q'}^{SB-GR}(\delta_T, \delta_R, \tau) + R_{pq,p'q'}^{DB}(\delta_T, \delta_R, \tau). \quad (35)$$

Note that we assume independence among the various components for simplicity, whereas in practice, some components may of course be correlated, e.g., the LoS and the SB-U component reflection from the UAV itself. Accounting for this is also a topic for future work.

By substituting (2) into (34), the space-time CF of the LoS component can be expressed as

$$R_{pq,p'q'}^{LoS}(\delta_T, \delta_R, \tau) = \frac{K}{K+1} e^{-j\frac{2\pi}{\lambda}(\varepsilon_{pq} - \varepsilon_{p'q'})} e^{j2\pi f_{Tm}\tau[\alpha_T^{LoS} - \gamma_T] \cos \beta_T^{LoS} \cos \xi + \sin \beta_T^{LoS} \sin \xi} e^{j2\pi f_{Rm}\tau[\cos(\alpha_R^{LoS} - \gamma_R) \cos \beta_R^{LoS}]} \quad (36)$$

where $\alpha_T^{LoS} \approx 0$, $\alpha_R^{LoS} \approx \pi$, and $\beta_T^{LoS} \approx \beta_R^{LoS} \approx \beta_0$.

In SB rays, due to the dependence between the AoD and AoA, we have

$$R_{pq,p'q'}^{\text{SB-U}}(\delta_T, \delta_R, \tau) = \frac{\eta_{\text{SB-U}}}{K+1} \int_{\beta_{R1}}^{\beta_{R2}} \int_{-\pi}^{\pi} f(\alpha_T) f(\beta_T) e^{-j\frac{2\pi}{\lambda}[(\varepsilon_{pn1} + \varepsilon_{n1q}) - (\varepsilon_{p'n1} + \varepsilon_{n1q'})]} e^{j2\pi f_{Tm}\tau [\cos(\alpha_T - \gamma_T) \cos \beta_T \cos \xi + \sin \beta_T \sin \xi]} e^{j2\pi f_{Rm}\tau [\cos(\alpha_R - \gamma_R) \cos \beta_R]} d\alpha_T d\beta_T \quad (37)$$

$$R_{pq,p'q'}^{\text{SB-G}}(\delta_T, \delta_R, \tau) = \frac{\eta_{\text{SB-G}}}{K+1} \int_{\beta_{R1}}^{\beta_{R2}} \int_{-\pi}^{\pi} f(\alpha_R) f(\beta_R) e^{-j\frac{2\pi}{\lambda}[(\varepsilon_{pn2} + \varepsilon_{n2q}) - (\varepsilon_{p'n2} + \varepsilon_{n2q'})]} e^{j2\pi f_{Tm}\tau [\cos(\alpha_T - \gamma_T) \cos \beta_T \cos \xi + \sin \beta_T \sin \xi]} e^{j2\pi f_{Rm}\tau [\cos(\alpha_R - \gamma_R) \cos \beta_R]} d\alpha_R d\beta_R \quad (38)$$

$$R_{pq,p'q'}^{\text{SB-GR}}(\delta_T, \delta_R, \tau) = \frac{\eta_{\text{SB-GR}}}{K+1} \int_0^{R_R} \int_{-\pi}^{\pi} f(\alpha_R) f(R) e^{-j\frac{2\pi}{\lambda}[(\varepsilon_{pn3} + \varepsilon_{n3q}) - (\varepsilon_{p'n3} + \varepsilon_{n3q'})]} e^{j2\pi f_{Tm}\tau [\cos(\alpha_T - \gamma_T) \cos \beta_T \cos \xi + \sin \beta_T \sin \xi]} e^{j2\pi f_{Rm}\tau [\cos(\alpha_R - \gamma_R) \cos \beta_R]} d\alpha_R dR. \quad (39)$$

The SB-GR rays occur on the bottom surface of the cylinder at the GS, i.e., in a 2-D area. In addition, there is a geometric relationship between the elevation AoA $\beta_R^{(n3)}$ and the radius R , i.e., $\tan \beta_R^{(n3)} = H_0/R$. Therefore, we can express the space-time CF of SB-GR rays by integrating the functions of the radius R and the azimuth AoA α_R .

The space-time CF of DB rays is

$$R_{pq,p'q'}^{\text{DB}}(\delta_T, \delta_R, \tau) = \frac{\eta_{\text{DB}}}{K+1} \int_{\beta_{R1}}^{\beta_{R2}} \int_{-\pi}^{\pi} \int_{\beta_{T1}}^{\beta_{T2}} \int_{-\pi}^{\pi} e^{-j\frac{2\pi}{\lambda}[(\varepsilon_{pn1} + \varepsilon_{n2q}) - (\varepsilon_{p'n1} + \varepsilon_{n2q'})]} e^{j2\pi f_{Tm}\tau [\cos(\alpha_T - \gamma_T) \cos \beta_T \cos \xi + \sin \beta_T \sin \xi]} e^{j2\pi f_{Rm}\tau [\cos(\alpha_R - \gamma_R) \cos \beta_R]} f(\alpha_T) f(\beta_T) f(\alpha_R) f(\beta_R) d\alpha_T d\beta_T d\alpha_R d\beta_R \quad (40)$$

which is a 4-D integral and thus difficult to solve. From the geometry, we determine that the degenerate spatial CFs of DB rays are exactly the same as those of SB rays. Specifically, we have $R_{pq,p'q'}^{\text{DB}}(\delta_T) = R_{pq,p'q'}^{\text{SB-U}}(\delta_T)$ and $R_{pq,p'q'}^{\text{DB}}(\delta_R) = R_{pq,p'q'}^{\text{SB-G}}(\delta_R)$. Therefore, to obtain the spatial part of (40), we only have to numerically calculate the 2-D integrals (37) and (38). Now, for the degenerate temporal CF of (40), by substituting in the azimuth angle densities and solving two integrals, its expression can be simplified as

$$R_{pq,pq}^{\text{DB}}(\tau) = \frac{\eta_{\text{DB}}}{K+1} \int_{\beta_{R1}}^{\beta_{R2}} \int_{-\pi}^{\pi} \int_{\beta_{T1}}^{\beta_{T2}} \int_{-\pi}^{\pi} f(\alpha_T) f(\beta_T) f(\alpha_R) f(\beta_R) e^{j2\pi f_{Tm}\tau [\cos(\alpha_T - \gamma_T) \cos \beta_T \cos \xi + \sin \beta_T \sin \xi]} e^{j2\pi f_{Rm}\tau [\cos(\alpha_R - \gamma_R) \cos \beta_R]} d\alpha_T d\beta_T d\alpha_R d\beta_R \\ = \frac{\eta_{\text{DB}}}{K+1} \int_{\beta_{R1}}^{\beta_{R2}} \int_{\beta_{T1}}^{\beta_{T2}} f(\beta_T) f(\beta_R) / I_0(k_T) / I_0(k_R)$$

$$I_0\left(\sqrt{k_T^2 + j2Q_T \cos(\gamma_T - \alpha_{T\mu}) - (Q_T)^2 \tau^2}\right) \\ I_0\left(\sqrt{k_R^2 + j2Q_R \cos(\gamma_R - \alpha_{R\mu}) - (Q_R)^2 \tau^2}\right) d\beta_T \\ \times d\beta_R \quad (41)$$

where $Q_T = 2\pi f_{Tm} \cos \beta_T \cos \xi$, $Q_R = 2\pi f_{Rm} \cos \beta_R$, and the integral is only 2-D now. The detailed derivation is in Appendix B.

B. Doppler PSD

The corresponding Doppler PSD can be obtained by using the Fourier transform of the space-time CF described above, with respect to τ , i.e., $R_{pq}(\tau)$, and can be expressed as

$$S_{pq}(f_D) = \int_{-\infty}^{\infty} R_{pq}(\tau) e^{-j2\pi f_D \tau} d\tau \quad (42)$$

where f_D is the Doppler frequency. Similar to (35), the expression of $S_{pq}(f_D)$ can also be written as

$$S_{pq}(f_D) = S_{pq}^{\text{LoS}}(f_D) + S_{pq}^{\text{SB-U}}(f_D) + S_{pq}^{\text{SB-G}}(f_D) \\ + S_{pq}^{\text{SB-GR}}(f_D) + S_{pq}^{\text{DB}}(f_D). \quad (43)$$

C. Envelope LCR

The LCR $L(r)$ is the expected number of times that the received signal level crosses a given threshold level r per second in the positive/negative direction. This quantifies the frequency of small-scale signal fading over the range of signal levels. The LCR of our model can be expressed as [40]

$$L(r) = \frac{2r\sqrt{K+1}}{\pi^{\frac{3}{2}}} \sqrt{\frac{b_2}{b_0} - \frac{b_1^2}{b_0^2}} \cdot e^{-K-(K+1)r^2} \\ \int_0^{\pi/2} \cosh\left(2\sqrt{K(K+1)}r \cos \theta\right) \\ \left[e^{-L(\chi \sin \theta)^2} + \sqrt{\pi} \chi \sin \theta \cdot \text{erf}(\chi \sin \theta)\right] d\theta \quad (44)$$

where $\cosh(\cdot)$ and $\text{erf}(\cdot)$ denote the hyperbolic cosine function and the error function, respectively, and $\chi = \sqrt{[(Kb_1^2)/(b_0b_2 - b_1^2)]}$. Parameters b_0 , b_1 , and b_2 are defined as

$$b_0 = \text{E}\left[h_{pq}^I(t)^2\right] = \text{E}\left[h_{pq}^Q(t)^2\right] \quad (45)$$

$$b_1 = \text{E}\left[h_{pq}^I(t)\dot{h}_{pq}^Q(t)\right] = \text{E}\left[h_{pq}^Q(t)\dot{h}_{pq}^I(t)\right] \quad (46)$$

$$b_2 = \text{E}\left[\dot{h}_{pq}^I(t)^2\right] = \text{E}\left[\dot{h}_{pq}^Q(t)^2\right] \quad (47)$$

where the in-phase and quadrature components of $h_{pq}(t)$ are represented by $h_{pq}^I(t)$ and $h_{pq}^Q(t)$, and the corresponding first derivative is denoted by $\dot{h}_{pq}^I(t)$ and $\dot{h}_{pq}^Q(t)$.

By substituting (1) to (45)–(47), parameters b_m ($m \in \{0, 1, 2\}$) become

$$b_m = b_m^{\text{SB-U}} + b_m^{\text{SB-G}} + b_m^{\text{SB-GR}} + b_m^{\text{DB}} \quad (48)$$

where

$$b_m^{\text{SB-U}} = \frac{\eta_{\text{SB-U}}}{2(K+1)} (2\pi)^m \int_{\beta_{T1}}^{\beta_{T2}} \int_{-\pi}^{\pi} f(\alpha_T) f(\beta_T)$$

$$\left\{ f_{Tm} [\cos(\alpha_T - \gamma_T) \cos \beta_T \cos \xi + \sin \beta_T \sin \xi] + f_{Rm} [\cos(\alpha_R - \gamma_R) \cos \beta_R] \right\}^m d\alpha_T d\beta_T \quad (49)$$

$$b_m^{SB-G} = \frac{\eta_{SB-G}}{2(K+1)} (2\pi)^m \int_{\beta_{R1}}^{\beta_{R2}} \int_{-\pi}^{\pi} f(\alpha_R) f(\beta_R) \left\{ f_{Tm} [\cos(\alpha_T - \gamma_T) \cos \beta_T \cos \xi + \sin \beta_T \sin \xi] + f_{Rm} [\cos(\alpha_R - \gamma_R) \cos \beta_R] \right\}^m d\alpha_R d\beta_R \quad (50)$$

$$b_m^{SB-GR} = \frac{\eta_{SB-GR}}{2(K+1)} (2\pi)^m \int_0^{R_R} \int_{-\pi}^{\pi} f(\alpha_R) f(R) \left\{ f_{Tm} [\cos(\alpha_T - \gamma_T) \cos \beta_T \cos \xi + \sin \beta_T \sin \xi] + f_{Rm} [\cos(\alpha_R - \gamma_R) \cos \beta_R] \right\}^m d\alpha_R dR \quad (51)$$

$$b_m^{DB} = \frac{\eta_{DB}}{2(K+1)} (2\pi)^m \int_{\beta_{R1}}^{\beta_{R2}} \int_{-\pi}^{\pi} \int_{\beta_{T1}}^{\beta_{T2}} \int_{-\pi}^{\pi} f(\alpha_T) f(\beta_T) f(\alpha_R) f(\beta_R) \times \left\{ f_{Tm} [\cos(\alpha_T - \gamma_T) \cos \beta_T \cos \xi + \sin \beta_T \sin \xi] + f_{Rm} [\cos(\alpha_R - \gamma_R) \cos \beta_R] \right\}^m d\alpha_T d\beta_T d\alpha_R d\beta_R. \quad (52)$$

Note that for $m = 0$, we have

$$b_0 = b_0^{SB-U} + b_0^{SB-G} + b_0^{SB-GR} + b_0^{DB} = \frac{1}{2(K+1)} \quad (53)$$

where

$$b_0^{SB-U} = \frac{\eta_{SB-U}}{2(K+1)} \int_{\beta_{T1}}^{\beta_{T2}} \int_{-\pi}^{\pi} f(\alpha_T) f(\beta_T) d\alpha_T d\beta_T = \frac{\eta_{SB-U}}{2(K+1)} \quad (54)$$

$$b_0^{SB-G} = \frac{\eta_{SB-G}}{2(K+1)} \int_{\beta_{R1}}^{\beta_{R2}} \int_{-\pi}^{\pi} f(\alpha_R) f(\beta_R) d\alpha_R d\beta_R = \frac{\eta_{SB-G}}{2(K+1)} \quad (55)$$

$$b_0^{SB-GR} = \frac{\eta_{SB-GR}}{2(K+1)} \int_0^{R_R} \int_{-\pi}^{\pi} f(\alpha_R) f(R) d\alpha_R dR = \frac{\eta_{SB-GR}}{2(K+1)} \quad (56)$$

$$b_0^{DB} = \frac{\eta_{DB}}{2(K+1)} \int_{\beta_{R1}}^{\beta_{R2}} \int_{-\pi}^{\pi} \int_{\beta_{T1}}^{\beta_{T2}} \int_{-\pi}^{\pi} f(\alpha_T) f(\beta_T) f(\alpha_R) f(\beta_R) d\alpha_T d\beta_T d\alpha_R d\beta_R = \frac{\eta_{DB}}{2(K+1)}. \quad (57)$$

D. Envelope AFD

The AFD $T(r)$ is defined as the average time over which the signal envelope $|h_{pq}(t)|$ remains below a certain level r [40], which can be written as

$$T(r) = \frac{1 - Q(\sqrt{2K}, \sqrt{2(K+1)r^2})}{L(r)} \quad (58)$$

where $Q(\cdot)$ is the Marcum Q function.

IV. NUMERICAL RESULTS AND ANALYSIS

We analyze numerically the derived statistical properties under different scattering environments in this section. First, we consider a low-altitude UAV communication scenario.

TABLE II
PARAMETERS USED IN FIGS. 2–9

Symbol	Fig.2	Fig.3	Fig.4	Fig.5	Fig.6	Fig.7	Fig.8	Fig.9
D	100	100	100	100	100	100	(a)1000 (b)300	1000
H_0	5	5	5	5	5	5	5	5
λ	0.1	0.1	0.1	0.1	0.1	0.1	0.1	0.1
R_T	5	5	5	5	5	5	(a)20 (b)50	20
R_R	3	3	3	3	3	3	(a)105 (b)80	105
β_0	(a) $\frac{\pi}{6}$ (b) $\frac{\pi}{3}$	(a) $\frac{\pi}{6}$ (b) $\frac{\pi}{4}$	(a) $\frac{\pi}{6}$ (b) $\frac{\pi}{3}$	(a) $\frac{\pi}{4}$ (b) $\frac{\pi}{2\sqrt{2}}$	$\frac{\pi}{3}$	$\frac{\pi}{6} - \frac{\pi}{3}$	(a) $\frac{\pi}{12}$ (b) $\frac{\pi}{6}$	$\frac{\pi}{10}$
θ_T θ_R	$\frac{\pi}{2}$ $\frac{\pi}{2}$	$\frac{\pi}{2}$ $\frac{\pi}{2}$	$\frac{\pi}{2}$ $\frac{\pi}{2}$	$\frac{\pi}{2}$ $\frac{\pi}{2}$	$0 - \frac{\pi}{2}$ $\frac{\pi}{2}$	$\frac{\pi}{2}$ $\frac{\pi}{2}$	$\frac{\pi}{2}$ $\frac{\pi}{2}$	$\frac{\pi}{2}$ $\frac{\pi}{2}$
v_T v_R	10 0.05	10 0.05	10 0.05	10 0.05	10 0.05	10 0.05	8 0	1 0
ξ	$0 - \frac{\pi}{4}$	$0 - \frac{\pi}{4}$	$0 - \frac{\pi}{4}$	$0 - \frac{\pi}{4}$	0	0	0	0
γ_T γ_R	$0 - \frac{\pi}{4}$ 0	$0 - \frac{\pi}{4}$ 0	$0 - \frac{\pi}{4}$ 0	$0 - \frac{\pi}{4}$ 0	0 0	0 0	$\frac{\pi}{11}$ $\frac{\pi}{11}$	$\frac{\pi}{11}$ 0
k_T	10	10	10	10	10	10	(a)1 (b)0.2	1
k_R	3	3	3	3	3	3	(a)0.5 (b)5.5	0.5
$\alpha_{T\mu}$	(a) $\frac{\pi}{4}$ (b) 0	π	(a) $\frac{\pi}{4}$ (b) 0	0	(a) 0 (b) 0 (c) $\frac{\pi}{2}$ (d) $\frac{\pi}{2}$	0	0	0
$\alpha_{R\mu}$	π	(a) π (b) $\frac{\pi}{2}$	π	π	(a) $\frac{\pi}{2}$ (b) $\frac{\pi}{2}$ (c) π (d) 0	π	π	π
$\beta_{T\mu}$	(a) $\frac{\pi}{4}$ (b) $\frac{\pi}{6}$	$\frac{\pi}{4}$	(a) 0 (b) $\frac{\pi}{6}$	0	0	0	0	$\frac{\pi}{4}$
$\beta_{R\mu}$	$\frac{\pi}{4}$	(a) $\frac{\pi}{4}$ (b) $\frac{\pi}{4}$	$\frac{\pi}{4}$	$\frac{\pi}{4}$	0	$\frac{\pi}{4}$	$\frac{\pi}{5}$	$\frac{\pi}{4}$
β_{Tm} β_{Rm}	$\frac{\pi}{6}$ $\frac{\pi}{6}$	$\frac{\pi}{6}$ $\frac{\pi}{6}$	$\frac{\pi}{6}$ $\frac{\pi}{6}$	$\frac{\pi}{6}$ $\frac{\pi}{6}$	$\frac{\pi}{6}$ $\frac{\pi}{6}$	$\frac{\pi}{6}$ $\frac{\pi}{6}$	$\frac{\pi}{6}$ $\frac{\pi}{6}$	$\frac{\pi}{6}$ $\frac{\pi}{6}$
K	0.03	0.03	0.03	0.03	0.03	0.3	(a)0.03 (b)0	0.03
η_{SB-U}	-	-	-	0.05	-	0.2	(a)0.05 (b)0.05	0.1
η_{SB-G}	-	-	-	0.85	-	0.4	(a)0.85 (b)0.9	0.7
η_{SB-GR}	-	-	-	0.05	-	0.3	(a)0.05 (b)0.05	0.15
η_{DB}	-	-	-	0.05	-	0.1	(a)0.05 (b)0	0.05

Table II lists the parameter values for different analyses, with results in Figs. 2–9. Note that we set the velocity of the GS as $v_R = 0.05$ m/s in this article because we want to focus on the effect of the UAV movement. Since $v_T \gg v_R$, the maximum Doppler shift can be written as $f_{D\max} = (v_T + v_R)/\lambda \approx v_T/\lambda = 100$ Hz. The scattering around the GS comes from houses, vehicles, lamps, trees, etc. The heights of these scatterers are approximately several meters. The scatterers near the UAV, which is near 50 m above the ground, would mostly emanate from taller buildings, and occasionally other aircraft.

Fig. 2 shows the absolute value of temporal CFs of SB-U and DB rays for different UAV moving directions in two scattering environments. From Fig. 2, the maximum value of the curve occurs at $\xi = \beta_{T\mu}$ and $\gamma_T = \alpha_{T\mu}$, which means that the UAV moves directly toward or away from the scatterer area densely distributed around the UAV. This is because there is minimal change in the propagation environment in this case, resulting in the two complex fading envelopes having the largest temporal correlation.

Next, we discuss and analyze whether the UAV moving direction has the same impact on temporal CFs of the SB-G and SB-GR rays. As shown in Fig. 3, different from the above conclusion, the maximum temporal correlation of the SB-G and SB-GR rays appears when $\xi = \beta_0$ and $\gamma_T = 0$, which can be seen from the model diagram as the movement of the UAV straight toward or directly away from the GS, i.e., the LoS component direction. Since the scatterers for the SB-G and SB-GR component are distributed primarily near

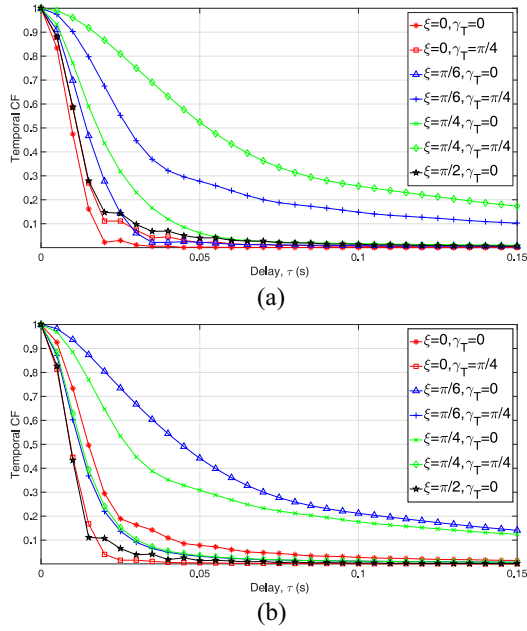


Fig. 2. (a) Temporal CFs of SB-U rays for different UAV moving directions with the environment parameters $\beta_0 = \pi/6$, $\beta_{T\mu} = \pi/4$, and $\alpha_{T\mu} = \pi/4$. (b) Temporal CFs of DB rays for different UAV moving directions with the environment parameters $\beta_0 = \pi/3$, $\beta_{T\mu} = \pi/6$, and $\alpha_{T\mu} = 0$.

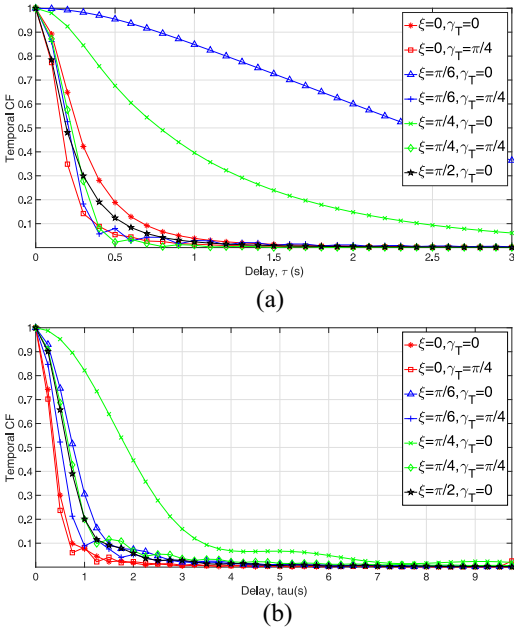


Fig. 3. (a) Temporal CFs of SB-G rays for different UAV moving directions with the environment parameters $\beta_0 = \pi/6$, $\beta_{R\mu} = \pi/4$, and $\alpha_{R\mu} = \pi$. (b) Temporal CFs of SB-GR rays for different UAV moving directions with the environment parameters $\beta_0 = \pi/4$ and $\alpha_{R\mu} = \pi/2$.

the GS and satisfy $D \gg R_R$, the different distribution of the scatterers is difficult to distinguish in this case.

From Figs. 2 and 3, we can see that the UAV moving direction has a significant influence on the temporal correlation. More importantly, Figs. 2 and 3 imply that the scatterers around the UAV dramatically decrease the temporal CFs compared with the scatterers around the GS. This observation can be obtained by comparing the scales of the abscissae.

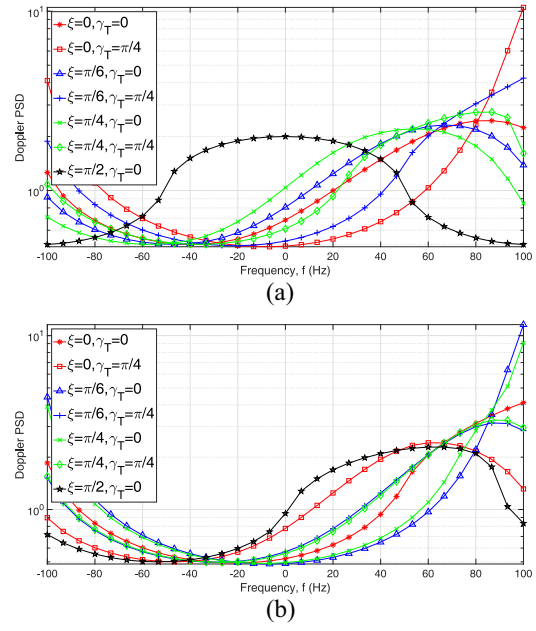


Fig. 4. Doppler PSDs of DB rays with different environment parameters. (a) $\beta_0 = \pi/6$, $\beta_{T\mu} = 0$, and $\alpha_{T\mu} = \pi/4$. (b) $\beta_0 = \pi/3$, $\beta_{T\mu} = \pi/6$, and $\alpha_{T\mu} = 0$.

Moreover, one can conclude that the scatterers around the UAV play a major role in the temporal CFs of DB rays.

Corresponding Doppler PSDs of DB rays when the UAV moves in different directions are shown in Fig. 4. When the UAV is moving toward or directly away from the scatterer-concentrated area, most of the power in the Doppler PSD is concentrated around the maximum Doppler frequency, i.e., $f_{D\max} = (v_T + v_R)/\lambda \approx v_T/\lambda$. In contrast, for other moving directions, e.g., $\xi = \pi/2$, the Doppler distributions are much wider than when the UAV is moving toward the scatterer-concentrated area. This observation shows that the shape of Doppler PSDs is dependent on the relationship between the scatterer distributions and UAV moving direction. Of course, we can use the formula $f_D = v_T \cos \theta / \lambda$, where θ is the angle between the propagating wave and the UAV's velocity, to estimate the components of Doppler frequencies and explain the different shapes of Doppler PSDs.

Fig. 5 represents the impact of the UAV's height on the absolute values of temporal CFs for different UAV moving directions. It can be noticed from Fig. 5 that when the angle β_0 increases, i.e., the height of the UAV's position increases, the difference among temporal CFs in the different UAV moving directions is reduced. As shown in Fig. 5(b), when $\beta_0 = \pi/2.2$, namely, $\tan \beta_0 \approx 7$, the differences among temporal CFs for different UAV moving directions have become negligible. Therefore, to reduce the impact of UAV moving directions on temporal CFs, a practical way is to elevate the UAV to a sufficient altitude. For example, as we have set $D = 100$ m, the estimated altitude in Fig. 5(b) is about $H = 700$ m.

In order to obtain robust MIMO performance, we usually want to obtain a large channel spatial diversity, which means that the spatial correlation is small [41]. In response to this, we

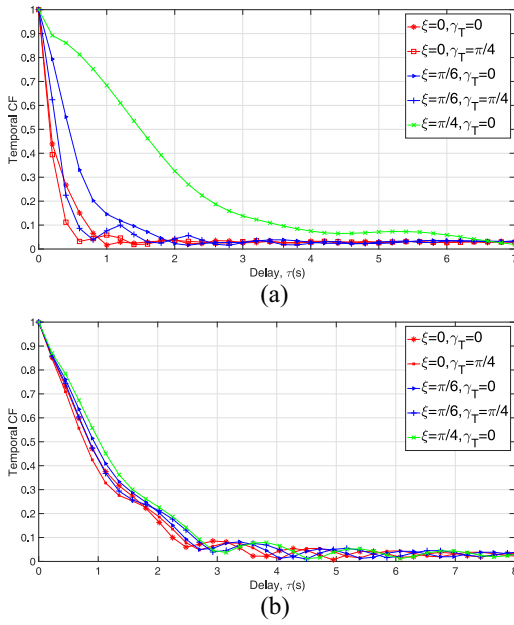


Fig. 5. Temporal CFs for different UAV moving directions with two UAV elevation angles. (a) $\beta_0 = \pi/4$. (b) $\beta_0 = \pi/2.2$.

discuss absolute values of spatial CFs of SB-U, SB-G, SB-GR, and DB components for different antenna orientations under four scattering environments at the UAV. Fig. 6 shows that the minimum spatial correlation at the UAV side is related to the antenna orientation θ_T and the average value of the azimuth angle of scatterers $\alpha_{T(R)\mu}$, and satisfies $|\theta_T - \alpha_{T(R)\mu}| = \pi/2$, i.e., the two angles are orthogonal. This conclusion can also be applied to UAV measurement activities to achieve better communication performance. It is clear that the antenna spacing has a significant impact on channel spatial correlations. Moreover, we can observe that compared with the spatial correlation of SB-G and SB-GR, the spatial correlation of SB-U and DB is much more sensitive to the antenna spacing at the UAV side. This means that the antenna spacing at the UAV side has a significant influence on the spatial correlations of SB-U and DB.

Next, Fig. 7 illustrates the influence of the height of the UAV on the channel second-order statistical characteristics, i.e., LCR and AFD, by adjusting the parameter β_0 . The figures show that when β_0 increases, the value of LCR decreases and the corresponding AFD increases. According to the geometric relationship, the linear distance between UAV and GS can be expressed as $d(\text{UAV}, \text{GS}) = D/\cos \beta_0$. When the UAV's altitude increases, the influence of the UAV movement decreases, resulting in an increase in the temporal stability of the channel, as one would expect intuitively.

Based on observations and discussions from Figs. 2–7, we can conclude some general rules for the control of the UAV to set up a robust UAV wireless communication system as follows.

- 1) In general, if at all possible, the UAV should first move to a relatively high altitude before starting to set up a UAV-assisted wireless communication system (as shown in Figs. 5 and 7). This is because the higher the UAV

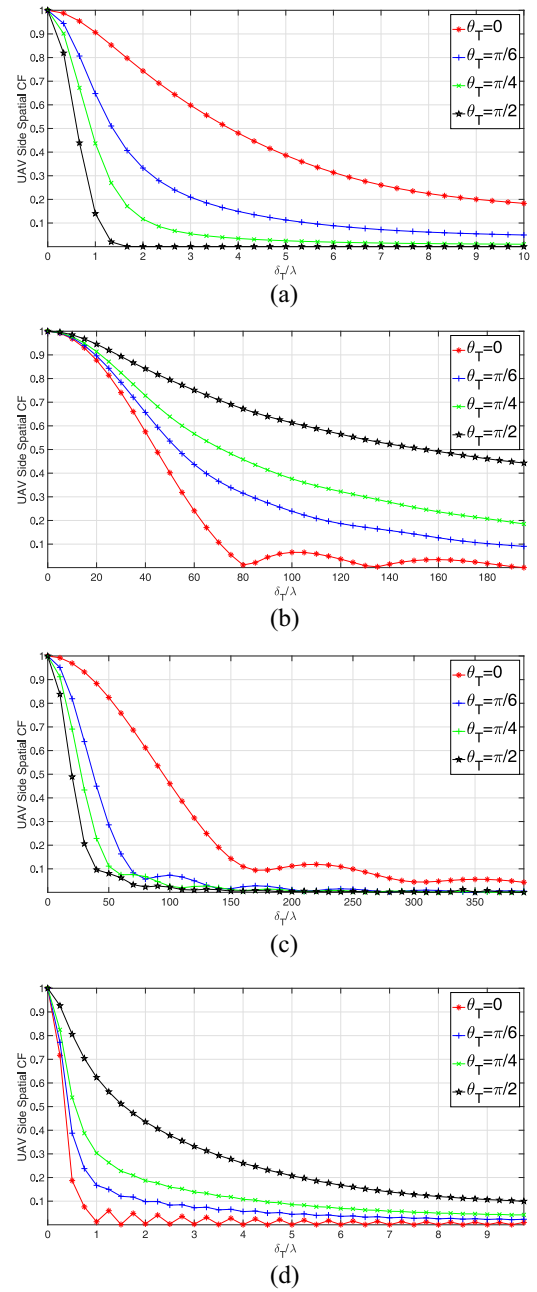


Fig. 6. UAV side spatial CFs for different antenna orientations under four scattering environments. (a) CFs of SB-U rays with $\alpha_{T\mu} = 0$. (b) CFs of SB-G rays with $\alpha_{R\mu} = \pi/2$. (c) CFs of SB-GR rays with $\alpha_{R\mu} = \pi$. (d) CFs of DB rays with $\alpha_{T\mu} = \pi/2$.

altitude, the better the temporal stability of UAV channels. Higher altitude also increases the probability of an LoS component in cluttered settings. Note that because of the increase of the channel path loss with altitude, the higher altitude of the UAV is only necessarily better up to some maximum value.

- 2) Compared with the scatterers around the GS, the scatterers around the UAV have a dominant impact on the temporal correlation and can significantly increase the time variation of UAV channels (see Figs. 2 and 3). Therefore, if the UAV is in a dense scattering area, it

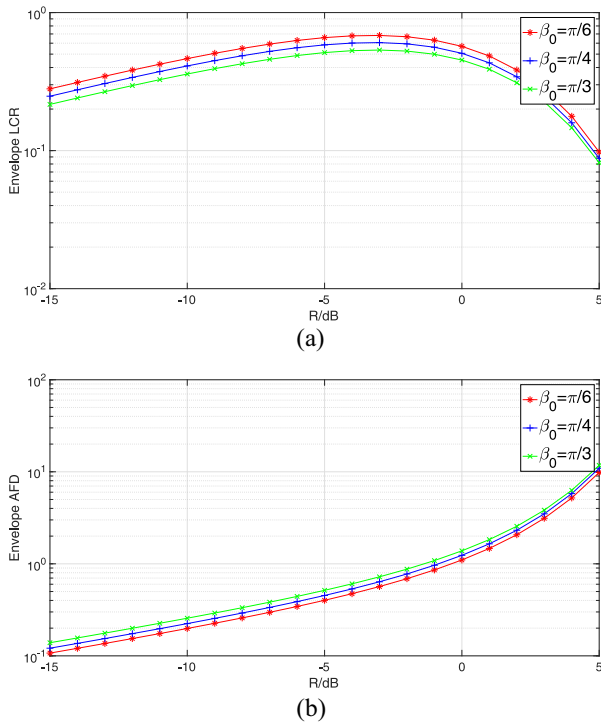


Fig. 7. Envelope (a) LCR and (b) AFD for different elevation angles of the UAV.

would be better to control the UAV to leave that area in order to achieve more stable propagation conditions.

- 3) For the scenario where the UAV is surrounded by many scatterers, the UAV should move directly away from the scatterer-concentrated area. In this case, the UAV not only follows rule 2) but also the UAV channel has the maximum temporal correlation and thus exhibits the best stability (as shown in Fig. 2). For some scenarios where the UAV is free of scatterers, i.e., the SB-G and SB-GR dominant environments, the UAV simply needs to move along the LoS direction in order to achieve the most stable propagation condition (as shown in Fig. 3).
- 4) For achieving better MIMO performance, the UAV should adjust the antenna orientation to achieve orthogonality with the mean angle of scatterers. In this case, the UAV channel has minimum spatial correlation and thus exhibits the maximum spatial diversity (as shown in Fig. 6).

Rule 1) is useful to achieve reliable communication performance because in this case, the flight altitude and moving directions of the UAV have a negligible impact on the channel statistics. Rules 2) and 3) are useful to achieve reliable communication performance by maintaining a large temporal correlation of the UAV channel, whereas rule 4) is useful to achieve better MIMO performance when the UAV has multiple antennas.

Figs. 8 and 9 compare theoretical results based on our model with the available measurement data. Before going into detailed analysis, we first summarize the general steps and rules about how to properly select model parameters. First, one can select the basic environment-related parameters,

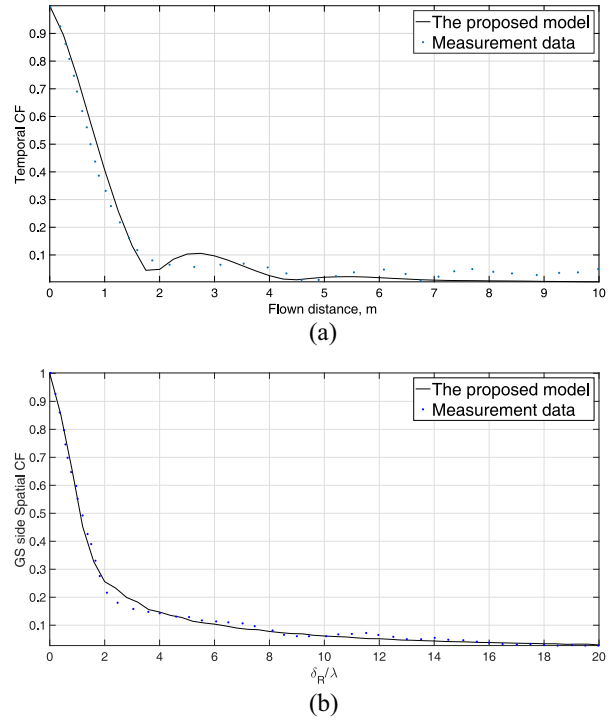


Fig. 8. Comparisons between the theoretical CFs and the measurement data. (a) Temporal CF. (b) Space CF at the GS side.

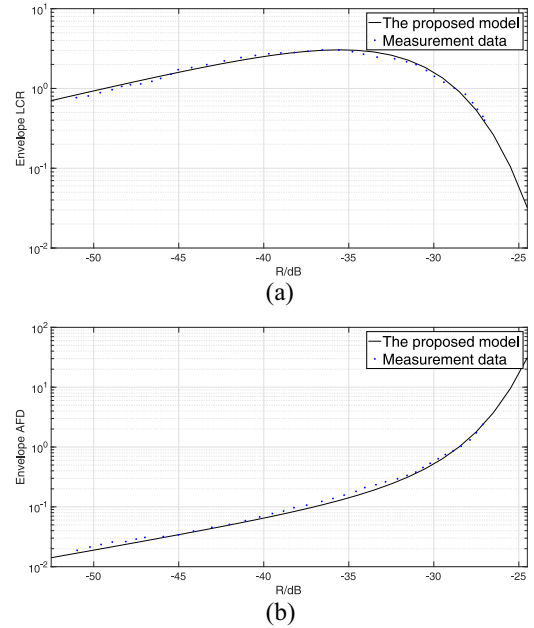


Fig. 9. Comparisons between the theoretical (a) LCR and (b) AFD, and the measurement data.

e.g., the distance between UAV and GS, and UAV-related parameters, e.g., the UAV's altitude, velocity, and movement direction, based on either the real measurement campaign (if one has measurement data) or the scenarios one expects. Second, according to the actual propagation environment or the expected environment, and the understanding of the proposed model, one can estimate the range of some important parameters, e.g., cylinders' radii, mean angles, energy-related

parameters, and Ricean factor. In general, the larger the distance between the UAV and the GS, the smaller the Ricean factor. However, this parameter will need “tuning” or refinement. For UAV scenarios with an LoS component, the Ricean factor dominates the main received power, whereas for non-LoS scenarios, energy-related parameters become dominant. For most UAV scenarios, where the UAV is, in general, away from scatterers, energy-related parameters η_{SB-G} and η_{SB-GR} correspond to the majority of the scattered power. The energy-related parameters η_{SB-U} and η_{DB} become dominant for scenarios with many scatterers near the UAV. Finally, based on the link range, one can easily set all model parameters to either match well with measurements or mimic channel properties of the expected environment.

Fig. 8 shows comparisons of some available measurement data with theoretical CFs of the proposed model. The temporal correlation’s measurement data comes from a low-elevation UAV channel measurement in [24]. Based on the actual measurement scenarios in [24] and [39], we determine some environment-related and UAV-related parameters, while the remaining parameters were estimated according to the general rules given in the last paragraph. All parameter values are listed in Table II. Note that here we use the flown distance (the product of the UAV velocity and flown time) in place of the correlation time to correspond with the description in [24]. In Fig. 8(b), we matched the theoretical GS side spatial CFs with some measurement data from [39]. Reference [39] considered an air-to-ground communication with antennas placed on ground and roof, respectively. Although this measurement did not use UAVs, it can be considered as a good reference for hovering UAV air-to-ground communication.

Fig. 9 presents the comparison between the measurement data from [24] and the theoretical LCR and AFD. It is worth pointing out that the measured path gain has been considered when obtaining theoretical values of LCR and AFD [24]. As shown in Figs. 8 and 9, theoretical results and the measured data are well matched, helping validate the practicability of our model.

Note that it is, in general, quite challenging to properly set these model parameters in order to obtain such excellent agreement. The model parameters should be properly chosen according to real communication scenarios, as well as a detailed understanding of the proposed model. In general, the close agreement is sensitive to several important model parameters, e.g., scattering-related parameters, such as $\alpha_{T\mu}$, $\beta_{T\mu}$, $\alpha_{R\mu}$, and $\beta_{R\mu}$, UAV-related parameters, such as the UAV moving direction, UAV altitude, and UAV antenna array orientation, and power-related parameters, such as η_{SB-U} , η_{SB-G} , η_{SB-GR} , and η_{DB} .

V. CONCLUSION

In this article, we have proposed a generic GBSM for UAV-MIMO Ricean fading channels. This model can be adaptable to various UAV environments by adjusting model parameters. From the proposed model, we have derived the space-time CF, the corresponding Doppler PSD, envelope LCR, and AFD for several UAV scattering environments. Based on the derived

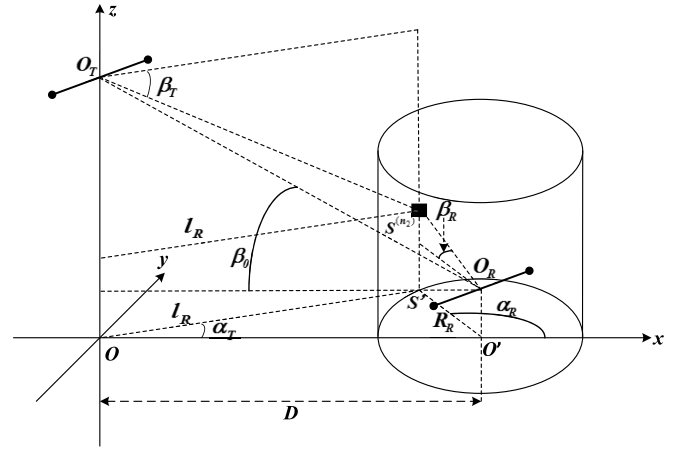


Fig. 10. Geometry of the proposed GBSM for SB-G rays.

statistical properties, we have further determined that a few UAV-related parameters (e.g., the UAV moving direction, UAV altitude, and antenna orientation) have a significant impact on the channel statistical properties. Accordingly, we have proposed some general rules for the UAV’s control to maintain the temporal stability of UAV channels and to obtain higher spatial diversity of UAV-MIMO channels. Finally, the practicality of our model was demonstrated by a good agreement between example measurement data and our theoretical results.

APPENDIX A DERIVATION OF (16)–(27)

Using the cosine theorem to $\triangle OS'O'$ in Fig. 10, we have

$$l_R^2 = R_R^2 + D^2 + 2R_R D \cos \alpha_R. \quad (59)$$

Note that for simplicity, we omit the superscript $(\cdot)^{(n_2)}$ in the above equation and following derivations. Since $R_R \ll D$, i.e., $R_R/D \ll 1$, l_R can be derived as

$$\begin{aligned} l_R &= D \sqrt{1 + 2 \frac{R_R}{D} \cos \alpha_R + \left(\frac{R_R}{D}\right)^2} \\ &\approx D \sqrt{1 + 2 \frac{R_R}{D} \cos \alpha_R} \\ &\approx D \left(1 + \frac{1}{2} \cdot 2 \frac{R_R}{D} \cos \alpha_R\right) \\ &= D + R_R \cos \alpha_R. \end{aligned} \quad (60)$$

By using the law of sines, we have

$$\sin \alpha_T \approx \frac{R_R}{l_R} \sin \alpha_R = \frac{\frac{R_R}{D} \sin \alpha_R}{1 + \frac{R_R}{D} \cos \alpha_R} \quad (61)$$

$$\cos \alpha_T \approx 1. \quad (62)$$

From the z -axis, we can get

$$D \tan \beta_0 = l_R \tan \beta_T + R_R \tan \beta_R. \quad (63)$$

Therefore

$$\tan \beta_T = \frac{D \tan \beta_0 - R \tan \beta_R}{l_R} = \frac{\tan \beta_0 - \frac{R_R}{D} \tan \beta_R}{1 + \frac{R_R}{D} \cos \alpha_R}. \quad (64)$$

Then, $\cos \beta_T$ and $\sin \beta_T$ ($\beta_T \in (0, (\pi/2))$) can be obtained as

$$\cos \beta_T = \frac{1 + \frac{R_R}{D} \cos \alpha_R}{\sqrt{\left(\tan \beta_0 - \frac{R_R}{D} \tan \beta_R\right)^2 + \left(1 + \frac{R_R}{D} \cos \alpha_R\right)^2}} \quad (65)$$

$$\sin \beta_T = \frac{\tan \beta_0 - \frac{R_R}{D} \tan \beta_R}{\sqrt{\left(\tan \beta_0 - \frac{R_R}{D} \tan \beta_R\right)^2 + \left(1 + \frac{R_R}{D} \cos \alpha_R\right)^2}}. \quad (66)$$

Since $R_R/D \ll 1$, $(R_R/D)^2$ is very small. The expression of $\cos \beta_T$ can be approximated as

$$\begin{aligned} \cos \beta_T &\approx \frac{1 + \frac{R_R}{D} \cos \alpha_R}{\sqrt{\frac{1}{\cos^2 \beta_0} - 2\frac{R_R}{D} \tan \beta_R \tan \beta_0 + 2\frac{R_R}{D} \cos \alpha_R}} \\ &= \frac{\left(1 + \frac{R_R}{D} \cos \alpha_R\right) \cos \beta_0}{\sqrt{1 - 2\frac{R_R}{D} \cos^2 \beta_0 (\tan \beta_R \tan \beta_0 - \cos \alpha_R)}} \\ &\approx \cos \beta_0 \left(1 + \frac{R_R}{D} \cos \alpha_R\right) \\ &\quad \left[1 + \frac{R_R}{D} \cos^2 \beta_0 (\tan \beta_R \tan \beta_0 - \cos \alpha_R)\right] \\ &\approx \cos \beta_0 \left[1 + \frac{R_R}{D} \cos^2 \beta_0 \tan \beta_R \tan \beta_0 \right. \\ &\quad \left. + \left(\frac{R_R}{D} \cos \alpha_R - \frac{R_R}{D} \cos^2 \beta_0 \cos \alpha_R\right)\right] \\ &= \cos \beta_0 + \frac{R_R}{D} \sin \beta_0 \cos \beta_0 \\ &\quad \times (\tan \beta_R \cos \beta_0 + \cos \alpha_R \sin \beta_0). \end{aligned} \quad (67)$$

Also, the expression of $\sin \beta_T$ can be simplified to

$$\sin \beta_T \approx \sin \beta_0 - \frac{R_R}{D} \cos^2 \beta_0 \cdot (\tan \beta_R \cos \beta_0 + \cos \alpha_R \sin \beta_0). \quad (68)$$

Following a similar derivation, we can obtain (16)–(19) in the case of SB-U rays and (24)–(27) in the case of SB-GR rays.

APPENDIX B DERIVATION OF (41)

The expression of (40) can be rewritten as

$$\begin{aligned} R_{pq,pq}^{\text{DB}}(\tau) &= \frac{\eta_{\text{DB}}}{K+1} \int_{\beta_{R_1}}^{\beta_{R_2}} \int_{\beta_{T_1}}^{\beta_{T_2}} f(\beta_T) f(\beta_R) \\ &\quad \left\{ \int_{-\pi}^{\pi} \int_{-\pi}^{\pi} e^{j2\pi f_{Rm} \tau [\cos(\alpha_R - \gamma_R) \cos \beta_R]} \right. \\ &\quad \left. e^{j2\pi f_{Tm} \tau [\cos(\alpha_T - \gamma_T) \cos \beta_T \cos \xi + \sin \beta_T \sin \xi]} \right. \\ &\quad \left. \frac{e^{k_T \cos(\alpha_T - \alpha_{T\mu})}}{2\pi I_0(k_T)} \frac{e^{k_R \cos(\alpha_R - \alpha_{R\mu})}}{2\pi I_0(k_R)} d\alpha_T d\alpha_R \right\} \\ &\quad \times d\beta_T d\beta_R. \end{aligned} \quad (69)$$

We define the inner 2-D integrals as $A(\tau)$, i.e.,

$$A(\tau) = \int_{-\pi}^{\pi} \int_{-\pi}^{\pi} e^{j2\pi f_{Rm} \tau [\cos(\alpha_R - \gamma_R) \cos \beta_R]} e^{j2\pi f_{Tm} \tau [\cos(\alpha_T - \gamma_T) \cos \beta_T \cos \xi + \sin \beta_T \sin \xi]}$$

$$\frac{e^{k_T \cos(\alpha_T - \alpha_{T\mu})}}{2\pi I_0(k_T)} \frac{e^{k_R \cos(\alpha_R - \alpha_{R\mu})}}{2\pi I_0(k_R)} d\alpha_T d\alpha_R. \quad (70)$$

Using the equation $\int_{-\pi}^{\pi} e^{a \sin x + b \cos x} dx = 2\pi I_0(\sqrt{a^2 + b^2})$, we have

$$\begin{aligned} A(\tau) &= \int_{-\pi}^{\pi} \frac{1}{2\pi I_0(k_T)} e^{k_T \cos(\alpha_T - \alpha_{T\mu})} \\ &\quad e^{j2\pi f_{Tm} \tau [\cos(\alpha_T - \gamma_T) \cos \beta_T \cos \xi + \sin \beta_T \sin \xi]} d\alpha_T \\ &\quad \int_{-\pi}^{\pi} \frac{1}{2\pi I_0(k_R)} e^{k_R \cos(\alpha_R - \alpha_{R\mu})} \\ &\quad e^{j2\pi f_{Rm} \tau [\cos(\alpha_R - \gamma_R) \cos \beta_R]} d\alpha_R. \end{aligned} \quad (71)$$

We can rewrite (71) as

$$\begin{aligned} A(\tau) &= \frac{1}{2\pi I_0(k_T)} \frac{1}{2\pi I_0(k_R)} e^{j2\pi f_{Tm} \tau \sin \beta_T \sin \xi} \\ &\quad \int_{-\pi}^{\pi} e^{(j2\pi f_{Tm} \tau \cos \beta_T \cos \xi \sin \gamma_T + k \sin \alpha_{T\mu}) \sin \alpha_T} \\ &\quad e^{(j2\pi f_{Tm} \tau \cos \beta_T \cos \xi \cos \gamma_T + k \cos \alpha_{T\mu}) \cos \alpha_T} d\alpha_T \\ &\quad \int_{-\pi}^{\pi} e^{(j2\pi f_{Rm} \tau \cos \beta_R \sin \gamma_R + k_R \sin \alpha_{R\mu}) \sin \alpha_R} \\ &\quad e^{(j2\pi f_{Rm} \tau \cos \beta_R \cos \gamma_R + k_R \cos \alpha_{R\mu}) \cos \alpha_R} d\alpha_R \\ &= I_0\left(\sqrt{k_T^2 + j2Q_T \cos(\gamma_T - \alpha_{T\mu}) - (Q_T)^2 \tau^2}\right) / I_0(k_T) \\ &\quad I_0\left(\sqrt{k_R^2 + j2Q_R \cos(\gamma_R - \alpha_{R\mu}) - (Q_R)^2 \tau^2}\right) / I_0(k_R) \end{aligned} \quad (72)$$

where $Q_T = 2\pi f_{Tm} \cos \beta_T \cos \xi$ and $Q_R = 2\pi f_{Rm} \cos \beta_R$. Therefore, the expression of (69) simplifies to (41).

REFERENCES

- [1] Y. Zeng, R. Zhang, and T. J. Lim, "Wireless communications with unmanned aerial vehicles: Opportunities and challenges," *IEEE Commun. Mag.*, vol. 54, no. 5, pp. 36–42, May 2016.
- [2] L. Gupta, R. Jain, and G. Vaszkun, "Survey of important issues in UAV communication networks," *IEEE Commun. Surveys Tuts.*, vol. 18, no. 2, pp. 1123–1152, 2nd Quart., 2016.
- [3] D. W. Matolak, "Air-ground channels & models: Comprehensive review and considerations for unmanned aircraft systems," in *Proc. IEEE Aerosp. Conf.*, Mar. 2012, pp. 1–17.
- [4] M. T. Dabiri, H. Safi, S. Parsaeefard, and W. Saad, "Analytical channel models for millimeter wave UAV networks under hovering fluctuations," *IEEE Trans. Wireless Commun.*, vol. 19, no. 4, pp. 2868–2883, Apr. 2020.
- [5] S. Suman, S. Kumar, and S. De, "Impact of hovering inaccuracy on UAV-aided RFET," *IEEE Commun. Lett.*, vol. 23, no. 12, pp. 2362–2366, Dec. 2019.
- [6] S. Wu, C.-X. Wang, E.-H. M. Aggoune, M. M. Alwakeel, and X. You, "A general 3D non-stationary 5G wireless channel model," *IEEE Trans. Commun.*, vol. 66, no. 7, pp. 3065–3078, Jul. 2018.
- [7] C.-X. Wang, J. Bian, J. Sun, W. Zhang, and M. Zhang, "A survey of 5G channel measurements and models," *IEEE Commun. Surveys Tuts.*, vol. 20, no. 4, pp. 3142–3168, 4th Quart., 2018.
- [8] J. Romeu, A. Aguiasca, J. Alonso, S. Blanch, and R. R. Martins, "Small UAV radiocommunication channel characterization," in *Proc. EuCAP*, Barcelona, Spain, Apr. 2010, pp. 1–5.
- [9] H. T. Kung, C.-K. Lin, T.-H. Lin, S. J. Tarsa, and D. Vlah, "Measuring diversity on a low-altitude UAV in a ground-to-air wireless 802.11 mesh network," in *Proc. IEEE GLOBECOM Workshops*, Dec. 2010, pp. 1799–1804.
- [10] E. Yanmaz, R. Kuschig, and C. Bettstetter, "Channel measurements over 802.11a-based UAV-to-ground links," in *Proc. IEEE GLOBECOM Workshops*, Houston, TX, USA, Dec. 2011, pp. 1280–1284.

- [11] M. Simunek, F. P. Fontán, P. Pecháč, and F. J. D. Otero, "Space diversity gain in urban area low elevation links for surveillance applications," *IEEE Trans. Antennas Propag.*, vol. 61, no. 12, pp. 6255–6260, Dec. 2013.
- [12] K. Takizawa, T. Kagawa, S. Lin, F. Ono, H. Tsuji, and R. Miura, "C-band aircraft-to-ground (A2G) radio channel measurement for unmanned aircraft systems," in *Proc. WPMC*, Sep. 2014, pp. 754–758.
- [13] J. Zelený, F. Pérez-Fontán, and P. Pecháč, "Initial results from a measurement campaign for low elevation angle links in different environments," in *Proc. EuCAP*, Lisbon, Portugal, May 2015, pp. 1–4.
- [14] T. J. Willink, C. C. Squires, G. W. K. Colman, and M. T. Muccio, "Measurement and characterization of low-altitude air-to-ground MIMO channels," *IEEE Trans. Veh. Technol.*, vol. 65, no. 4, pp. 2637–2648, Apr. 2016.
- [15] R. Guay, G. Drolet and J. R. Bray, "Measurement and modelling of the dynamic radar cross-section of an unmanned aerial vehicle," *IET Radar Sonar Navig.*, vol. 11, no. 7, pp. 1155–1160, Jul. 2017.
- [16] R. Amorim, H. Nguyen, P. Mogensen, I. Z. Kovács, J. Wigard, and T. B. Sørensen, "Radio channel modeling for UAV communication over cellular networks," *IEEE Wireless Commun. Lett.*, vol. 6, no. 4, pp. 514–517, Aug. 2017.
- [17] D. W. Matolak and R. Sun, "Air-ground channel characterization for unmanned aircraft systems—Part I: Methods, measurements, and models for over-water settings," *IEEE Trans. Veh. Technol.*, vol. 66, no. 1, pp. 26–44, Jan. 2017.
- [18] R. Sun and D. W. Matolak, "Air-ground channel characterization for unmanned aircraft systems—Part II: Hilly & mountainous settings," *IEEE Trans. Veh. Technol.*, vol. 66, no. 3, pp. 1913–1925, Mar. 2017.
- [19] D. W. Matolak and R. Sun, "Air-ground channel characterization for unmanned aircraft systems—Part III: The suburban and near-urban environments," *IEEE Trans. Veh. Technol.*, vol. 66, no. 8, pp. 6607–6618, Aug. 2017.
- [20] R. Sun, D. W. Matolak, and W. Rayess, "Air-ground channel characterization for unmanned aircraft systems—Part IV: Airframe shadowing," *IEEE Trans. Veh. Technol.*, vol. 66, no. 9, pp. 7643–7652, Sep. 2017.
- [21] K. Daniel, M. Putzke, B. Dusza, and C. Wietfeld, "Three dimensional channel characterization for low altitude aerial vehicles," in *Proc. ISWCS*, York, U.K., Sep. 2010, pp. 756–760.
- [22] Y. Wu *et al.*, "Ray tracing based wireless channel modeling over the sea surface near Diaoyu islands," in *Proc. CCITSA*, Ilan, Taiwan, Dec. 2015, pp. 124–128.
- [23] Z. Shi, P. Xia, Z. Gao, L. Huang, and C. Chen, "Modeling of wireless channel between UAV and vessel using the FDTD method," in *Proc. WiCOM*, Beijing, China, Sep. 2014, pp. 100–104.
- [24] M. Simunek, F. P. Fontán, and P. Pecháč, "The UAV low elevation propagation channel in urban areas: Statistical analysis and time-series generator," *IEEE Trans. Antennas Propag.*, vol. 61, no. 7, pp. 3850–3858, Jul. 2013.
- [25] N. Goddemeier and C. Wietfeld, "Investigation of air-to-air channel characteristics and a UAV specific extension to the rice model," in *Proc. IEEE GLOBECOM Workshops*, San Diego, CA, USA, Dec. 2015, pp. 1–5.
- [26] H. Chang, J. Bian, C.-X. Wang, Z. Bai, W. Zhou, and H. Aggoune, "A 3D non-stationary wideband GBSM for low-altitude UAV-to-ground V2V MIMO channels," *IEEE Access*, vol. 7, pp. 70719–70732, 2019.
- [27] A. A. Khuwaja, Y. Chen, N. Zhao, M. Alouini, and P. Dobbins, "A survey of channel modeling for UAV communications," *IEEE Commun. Surveys Tuts.*, vol. 20, no. 4, pp. 2804–2821, 4th Quart., 2018.
- [28] A. G. Zajic and G. L. Stuber, "Three-dimensional modeling, simulation, and capacity analysis of space-time correlated mobile-to-mobile channels," *IEEE Trans. Veh. Technol.*, vol. 57, no. 4, pp. 2042–2054, Jun. 2008.
- [29] A. G. Zajic, G. L. Stuber, T. G. Pratt, and S. T. Nguyen, "Wideband MIMO mobile-to-mobile channels: Geometry-based statistical modeling with experimental verification," *IEEE Trans. Veh. Technol.*, vol. 58, no. 2, pp. 517–534, Feb. 2009.
- [30] A. G. Zajic and G. L. Stuber, "Three-dimensional modeling and simulation of wideband MIMO mobile-to-mobile channels," *IEEE Trans. Wireless Commun.*, vol. 8, no. 3, pp. 1260–1275, Mar. 2009.
- [31] P. Liu, B. Ai, D. W. Matolak, R. Sun, and Y. Li, "5-GHz vehicle-to-vehicle channel characterization for example overpass channels," *IEEE Trans. Veh. Technol.*, vol. 65, no. 8, pp. 5862–5873, Aug. 2016.
- [32] R. He, B. Ai, G. L. Stuber, G. Wang, and Z. Zhong, "Geometrical based modeling for millimeter wave MIMO mobile-to-mobile channels," *IEEE Trans. Veh. Technol.*, vol. 67, no. 4, pp. 2848–2863, Apr. 2018.
- [33] J. Bian *et al.*, "A 3D wideband non-stationary multi-mobility model for vehicle-to-vehicle MIMO channels," *IEEE Access*, vol. 7, pp. 32562–32577, 2019.
- [34] Y. Yuan, C.-X. Wang, Y. He, M. M. Alwakeel, and H. Aggoune, "3D wideband non-stationary geometry-based stochastic models for non-isotropic MIMO vehicle-to-vehicle channels," *IEEE Trans. Wireless Commun.*, vol. 14, no. 12, pp. 6883–6895, Dec. 2015.
- [35] L. Zeng, X. Cheng, C.-X. Wang, and X. Yin, "A 3D geometry-based stochastic channel model for UAV-MIMO channels," in *Proc. WCNC*, San Francisco, CA, USA, Mar. 2017, pp. 1–5.
- [36] L. Zeng, X. Cheng, C.-X. Wang, and X. Yin, "Second order statistics of non-isotropic UAV Ricean fading channels," in *Proc. IEEE VTC-Fall*, Sep. 2017, pp. 1–5.
- [37] X. Cheng and Y. Li, "A 3D geometry-based stochastic model for UAV-MIMO wideband non-stationary channels," *IEEE Internet Things J.*, vol. 6, no. 2, pp. 1654–1662, Apr. 2019.
- [38] K. Jin, X. Cheng, X. Ge, and X. Yin, "Three dimensional modeling and space-time correlation for UAV channels," in *Proc. IEEE VTC-Spring*, Sydney, NSW, Australia, Jun. 2017, pp. 1–5.
- [39] S. Payami and F. Tufvesson, "Channel measurements and analysis for very large array systems at 2.6 GHz," in *Proc. EuCAP*, Prague, Czech Republic, Mar. 2012, pp. 433–437.
- [40] X. Cheng, C.-X. Wang, B. Ai, and H. Aggoune, "Envelope level crossing rate and average fade duration of nonisotropic vehicle-to-vehicle Ricean fading channels," *IEEE Trans. Intell. Transp. Syst.*, vol. 15, no. 1, pp. 62–72, Feb. 2014.
- [41] F. Bohagen, P. Orten, and G. E. Oien, "Design of optimal high-rank line-of-sight MIMO channels," *IEEE Trans. Wireless Commun.*, vol. 6, no. 4, pp. 1420–1425, Apr. 2007.



Xiang Cheng (Senior Member, IEEE) received the Ph.D. degree from Heriot-Watt University, Edinburgh, U.K., and the University of Edinburgh, Edinburgh, U.K., in 2009.

He is currently a Professor with Peking University, Beijing, China. He has published more than 200 journal and conference papers, six books, and holds ten patents. His general research interests are in the areas of channel modeling, wireless communications, and data analytics.

Prof. Cheng was a recipient of the IEEE Asia-Pacific Outstanding Young Researcher Award in 2015, and the co-recipient of the IEEE JSAC Best Paper Award: Leonard G. Abraham Prize in 2016, the NSFC Outstanding Young Investigator Award, and the First-Rank and Second-Rank Award in Natural Science, Ministry of Education, in China. He has also received the Best Paper Awards at IEEE ITST'12, ICC'13, ITSC'14, ICC'16, ICNC'17, GLOBECOM'18, ICCS'18, and ICC'19. He has served as the symposium leading chair, the co-chair, and a member of the Technical Program Committee for several international conferences. He is currently an Associate Editor of the IEEE TRANSACTIONS ON WIRELESS COMMUNICATIONS, the IEEE TRANSACTIONS ON INTELLIGENT TRANSPORTATION SYSTEMS, IEEE WIRELESS COMMUNICATIONS LETTERS, and the *Journal of Communications and Information Networks*, and is an IEEE Distinguished Lecturer.



Yiran Li received the B.S. degree in communication engineering from Northeastern University, Shenyang, China, in 2017. She is currently pursuing the master's degree with the School of Software and Microelectronics, Peking University, Beijing, China.

Her current research interests include channel modeling and vehicular communications.



Cheng-Xiang Wang (Fellow, IEEE) received the B.Sc. and M.Eng. degrees in communication and information systems from Shandong University, Jinan, China, in 1997 and 2000, respectively, and the Ph.D. degree in wireless communications from Aalborg University, Aalborg, Denmark, in 2004.

He was a Research Assistant with the Hamburg University of Technology, Hamburg, Germany, from 2000 to 2001, a Visiting Researcher with Siemens AG Mobile Phones, Munich, Germany, in 2004, and a Research Fellow with the University of Agder,

Grimstad, Norway, from 2001 to 2005. He has been with Heriot-Watt University, Edinburgh, U.K., since 2005, where he was promoted to a Professor in 2011. In 2018, he joined Southeast University, Nanjing, China, as a Professor. He is also a part-time Professor with Purple Mountain Laboratories, Nanjing. He has authored four books, one book chapter, and more than 380 papers in refereed journals and conference proceedings, including 23 highly cited papers. He has also delivered 20 invited keynote speeches/talks and seven tutorials in international conferences. His current research interests include wireless channel measurements and modeling, B5G wireless communication networks, and applying artificial intelligence to wireless communication networks.

Prof. Wang received the ten Best Paper Awards from IEEE GLOBECOM 2010, IEEE ICCT 2011, ITST 2012, IEEE VTC 2013-Spring, IWCMC 2015, IWCMC 2016, IEEE/CIC ICC 2016, WPMC 2016, and WOCC 2019. He received the Highly Cited Researcher recognized by Clarivate Analytics from 2017 to 2019. He has served as an Editor for nine international journals, including the IEEE TRANSACTIONS ON WIRELESS COMMUNICATIONS from 2007 to 2009, the IEEE TRANSACTIONS ON VEHICULAR TECHNOLOGY from 2011 to 2017, and the IEEE TRANSACTIONS ON COMMUNICATIONS from 2015 to 2017. He was a Guest Editor for the IEEE JOURNAL ON SELECTED AREAS IN COMMUNICATIONS, Special Issue on Vehicular Communications and Networks (Lead Guest Editor), Special Issue on Spectrum and Energy Efficient Design of Wireless Communication Networks, and Special Issue on Airborne Communication Networks. He was also a Guest Editor for the IEEE TRANSACTIONS ON BIG DATA, Special Issue on Wireless Big Data, and is a Guest Editor for the IEEE TRANSACTIONS ON COGNITIVE COMMUNICATIONS AND NETWORKING, Special Issue on Intelligent Resource Management for 5G and Beyond. He has served as a TPC member, a TPC chair, and the general chair for over 80 international conferences. He is a Fellow of IET, and an IEEE Communications Society Distinguished Lecturer in 2019 and 2020. He is currently an Executive Editorial Committee Member of the IEEE TRANSACTIONS ON WIRELESS COMMUNICATIONS.



Xuefeng Yin (Member, IEEE) received the B.S. degree in optoelectronics engineering from the Huazhong University of Science and Technology, Wuhan, China, in 1995, and the M.Sc. degree in digital communications and the Ph.D. degree in wireless communications from Aalborg University, Aalborg, Denmark, in 2002 and 2006, respectively.

From 2006 to 2008, he was an Assistant Professor with Aalborg University. In 2008, he joined the College of Electronics and Information Engineering, Tongji University, Shanghai, China, where he

became a Full Professor in 2016 and has been the Vice Dean since 2016. He has authored or coauthored more than 130 technical articles, four books, and 12 PCT patents. His research interests include high-resolution parameter estimation for propagation channels, measurement-based channel characterization, random propagation-graph-based channel simulations, radar signal processing, and target recognition assisted with deep learning techniques.

David W. Matolak (Senior Member, IEEE) received the B.S. degree in electrical engineering from Pennsylvania State University, State College, PA, USA, in 1983, the M.S. degree in electrical engineering from the University of Massachusetts, Boston, MA, USA, in 1987, and the Ph.D. degree in electrical engineering from the University of Virginia, Charlottesville, VA, USA, in 1995.

He has over 25 years' experience in communication system research, development, and deployment, with industry, government institutions, and academia, including AT&T Bell Labs, Murray Hill, NY, USA; L3 Communication Systems, New York NY, USA; MITRE, McLean, VA, USA; and Lockheed Martin, Bethesda, MD, USA. He was a Professor with Ohio University, Athens, OH, USA, from 1999 to 2012. Since 2012, he has been a Professor with the University of South Carolina, Columbia, SC, USA. He has over 250 publications and eight patents. His research interests are radio channel modeling and communication techniques for nonstationary fading channels.

Dr. Matolak has organized multiple IEEE workshops and special sessions, and is an Associate Editor of the IEEE TRANSACTIONS ON WIRELESS COMMUNICATIONS. He is also a member of standards groups in RTCA and ITU, and a member of Eta Kappa Nu, Sigma Xi, Tau Beta Pi, URSI, ASEE, and AIAA.